H3K9 methylation-independent activity for HPL-2/HP1 in heterochromatin foci, gene repression, and organogenesis

Colin E. Delaney,[1] Jia Emil You,[1] Susan M. Gasser[2], Jan Padeken[3#], and Susan E. Mango[1#]

1. University of Basel Biozentrum, Basel, Switzerland
2. Fondation ISREC, Lausanne, Switzerland
3. Institute for Molecular Biology (IMB), Mainz, Germany

Corresponding author

Abstract

In differentiated cells, genome segregation into heterochromatin and euchromatin is mediated by modified histones, which recruit so-called reader proteins. Surprisingly, many histone modifiers remain functional in the absence of catalytic activity, but the underlying mechanism remains unclear. To explore this puzzle, we examined the relationship between *C. elegans* MET-2/SETDB1, a histone H3 lysine (H3K9me) methyltransferase that also has non-catalytic roles, and the canonical H3K9me reader HPL-2 (HP1). We show that HPL-2 represses transcription and supports organogenesis independently of H3K9me binding, whereas complete loss of *met-2* and *hpl-2* causes severe transcriptional and developmental defects. MET-2 and HPL-2 rely on different binding partners - the disordered protein LIN-65/ATF7IP and the multi-zinc finger protein LIN-13, respectively – for localization and function. The results suggest that HPL-2 can operate through alternative protein interactions, and that HPL-2 and MET-2 function in parallel, H3K9me-independent pathways, with H3K9me acting as a reinforcing but non-essential contributor to these processes.

Introduction

Tissue differentiation in multicellular organisms is accompanied by the segregation of the genome into euchromatin and heterochromatin. Open euchromatin is accessible to transcriptional activators while compacted heterochromatin restricts transcription and relocates to the nuclear periphery and nucleolus (1). Distinct sets of post-translational modifications of histones (PTMs) are enriched in these genomic compartments and play important roles in transcriptional regulation. Methylation of histone H3 on lysine 9 (H3K9me) is a hallmark of transcriptionally silenced heterochromatin, marking satellite and simple repeats, transposable elements, and inactive tissue-specific genes (2). Loss of H3K9me-specific lysine methyltransferases (HMTs) that write H3K9me via their SET domains (Suppressor of Variegation, Enhancer of Zeste, Trithorax domain) is associated with defects in tissue differentiation, aging, and altered tumor immunogenicity (3-8). Once H3K9me is deposited, reader proteins like the highly conserved HP1 (heterochromatin protein 1) bind specifically to H3K9me2/me3 via their chromodomain (9, 10). HP1 binding of H3K9me, followed by its dimerization via its chromoshadow domain, is a well-established model for heterochromatin compaction and gene silencing.

While the prevailing view suggests HP1 binds H3K9me to function, recent studies have suggested a more nuanced relationship. HP1 can interact with chromatin through H3K9me binding but also via DNA and RNA binding to the hinge domain (11-14), and single molecule live imaging demonstrates dynamic H3K9me-independent HP1-nucleosome interactions (15). These observations suggest H3K9me independent activities, but to what extent PTM-dependent and -independent mechanisms contribute to HP1 function remains unclear. Whether or how H3K9me-independent interactions are linked to the demonstrated ability of HP1 to phase-separate in vitro, and show condensate-like fusing of foci in vivo, is a subject of active investigation (16-18).

In the nematode *C. elegans*, the relationship between HP1 homolog HPL-2 and H3K9me is similarly ill defined. HPL-2, MET-2/SETDB1, and H3K9me2 map to the same areas of the genome and repress repetitive elements in whole animal ChIP-seq experiments (19). However, overexpressed HPL-2 can bind target loci in embryos lacking all H3K9me, albeit at a weaker level (20). Further, HPL-2 acts redundantly with the SETDB1 homolog MET-2 in germline stability and vulval cell differentiation, suggesting independent functions (21, 22). The histone methyltransferase MET-2 is required for H3K9me-mediated gene silencing (23, 24), but also possesses a catalytic-independent function that maintains hypoacetylation of heterochromatin, mitigates phenotypes associated with the loss of H3K9me, and retains the ability to repress some genes (25). During interphase MET-2 forms dynamic heterochromatic foci that are independent of H3K9me and instead rely on interaction with the largely unstructured protein LIN-65/ATF7IP (26-28). Interestingly, overexpressed HPL-2 has also been

reported to localize to sub-nuclear foci (29); however, it is unclear how MET-2/SETDB1, H3K9me deposition, and HPL-2/HP1 functionally interact in transcriptional silencing and tissue differentiation.

Here, we interrogate the relationship between HPL-2/HP1, H3K9me, and MET-2/SETDB1 in localization, gene silencing, protein dynamics, and tissue differentiation. We find that while HPL-2 co-localizes with MET-2 in subnuclear heterochromatic foci, their recruitment to these foci is independent from each other. The independent targeting to heterochromatin foci correlates with a redundant role of MET-2 and HPL-2 in gene repression and restricting cell fate. Strikingly, HPL-2 localization does not require H3K9me binding. Instead, HPL-2 localization depends on physical interaction with the multi-zinc finger protein LIN-13 mediated by the chromoshadow domain. H3K9me binding plays only a minor role in HPL-2 mediated transcriptional repression and is dispensable for cell fate. These findings argue that multivalent protein-protein interactions may constitute a generalizable mechanism for heterochromatin function as an additional layer of regulation to histone PTMs.

Results

MET-2 and HPL-2 colocalize and are independently recruited into heterochromatic foci

To begin dissecting the relationship between MET-2/SETDB1, H3K9me, and HPL-2/HP1, we asked if endogenous HPL-2 forms foci and if so, how MET-2 and HPL-2 foci interact by imaging live, prebean-stage *C. elegans* embryos. We monitored HPL-2 protein using a strain expressing HPL-2 CRISPR-tagged with mKate2 and 3xFLAG inserted into the unstructured hinge region (Figure 1A) (30). The *hpl-2* gene encodes 2 isoforms (31). The major isoform accounts for 93% of total protein and exhibits the typical HP1 structure of chromodomain (CD)-hinge-chromoshadow domain (CSD), while the less abundant isoform possesses an abbreviated CSD and an extended C terminus (Fig. 1A). The internal HPL-2::mKate2 fusion tags both isoforms.

HPL-2::mKate2 was constitutively nuclear and concentrated into subnuclear foci (Fig. 1B). We then co-expressed HPL-2::mKate2 with MET-2 endogenously tagged with mNeonGreen (32), and observed that HPL-2 foci to a large extent colocalized with MET-2 foci (Fig. 1B). Knockdown of either *met-2* or *hpl-2* led to the loss of green or red fluorescence, respectively, indicating that the signal was specific (Fig. 1C). Surprisingly, the depletion of *met-2* did not result in a loss of HPL-2 foci (Figure 1C). We previously showed that MET-2 foci form independent of H3K9me using a MET-2 mutant deficient in catalytic activity (*met-2-CD*) (25). Similarly, HPL-2 foci persisted in *met-2-CD* embryos (Fig. 1D). Loss of heterochromatin results in temperature-dependent sterility (19, 24, 33-35). We confirmed that the strain expressing HPL-2::mKate2 remained viable and fertile at 26°C unlike *hpl-2Δ* animals (Fig. 1E), indicating that HPL-2::mKate2 is functional and raising the question how foci may contribute to HPL-2 function.

Factors downstream of MET-2 in the H3K9me pathway, *set-25* and *lin-61* (36), were dispensable for both MET-2 and HPL-2 foci (Fig. S1A). Loss of *hpl-1*, another HP1-like gene, does not exhibit the somatic and germline physiological defects seen in *met-2* or *hpl-2* mutant animals (31), and *hpl-1* was not necessary for MET-2 or HPL-2 foci (Fig. S1A). Further, endogenously tagged HPL-1 was observed to be expressed at the minimum limit of detection in embryos, much lower than HPL-2 levels, prior to upregulation in late embryogenesis (Fig. S1B and data not shown, (30)). Therefore, we focused on HPL-2, finding that HPL-2 and MET-2 form foci independent of each other. This result suggests two parallel pathways for subnuclear localization of heterochromatin factors MET-2 and HPL-2.

MET-2 and HPL-2 repress transcription via parallel pathways

To begin dissecting how HPL-2 and MET-2's independent targeting to foci may correlate with their functions, we examined the effect of HPL-2 and MET-2 on transcription in *C. elegans* embryos. The well-characterized repetitive heterochromatic array *gwIs4* expresses nuclear GFP and is repressed by

MET-2, SET-25, and HPL-2 (37, 38). Double deletion of both *met-2* and *set-25* eliminates all detectable H3K9me and leads to desilencing of the array (Fig. 2A) (38). Knockdown of *hpl-2* using RNAi led to a significant increase in GFP expression not only in WT, but also in *met-2 set-25* double mutants (Fig. 2A), indicating that HPL-2 has a silencing function independent of H3K9me binding. Consistently, double deletion of *met-2* and *hpl-2* shows synthetic phenotypes, suggesting parallel functions (Fig. 2B and (21, 22)).

For a comprehensive view of endogenous gene expression, we performed RNAseq. We compared *met-2Δ* with *hpl-2Δ* mutant early embryos and found 1319 genes up-regulated in *met-2Δ* and 205 genes up-regulated in *hpl-2Δ* (Fig. 2C, FC = 2, FDR = 0.05). Remarkably, not many genes were shared between the two mutant backgrounds (4% of MET-2 and 27% of HPL-2 targets shared). Comparison of HPL-2 up-regulated genes with those of *set-25Δ* mutants, lacking all H3K9me3, showed a similar lack of overlap (Fig. S2A), as SET-25 represses the same genes as MET-2 (Fig. S2B). In mutants lacking H3K9me, gene activation is associated with increased histone acetylation (25). Western immunoblotting confirmed that H3K9ac and H3K27ac were upregulated in *met-2Δ* embryos, but we observed no change in acetylation of these H3 residues from WT in *hpl-2Δ* mutants (Figs. 2D-E). These data show that MET-2 and HPL-2 silence distinct cohorts of genes and have different effects on global acetylation levels.

We next tested whether *met-2Δ hpl-2Δ* double mutants function redundantly for transcriptional repression. We performed RNAseq on *met-2Δ hpl-2Δ* double mutant early embryos. Sterile double mutants are maternally rescued, so we were able to employ a fluidic sorting strategy to purify a population of fertile double mutants from which to isolate embryos (see Methods). We found 928 genes upregulated in *met-2Δ hpl-2Δ* embryos relative to WT (Fig. 2F-G, FC = 2, FDR 0.05). Of these 928 upregulated genes, 543 and 125 genes were previously seen upregulated in *met-2Δ* and *hpl-2Δ* single mutants, respectively. However, 352 (38.2%) genes were de-repressed only in double mutant embryos. We tested a subset of desilenced genes using qRT-PCR and confirmed synergistic upregulation in *met-2Δ hpl-2Δ* embryos (Fig. 2H), demonstrating that MET-2 and HPL-2 act redundantly to repress certain genes. We also observed certain repeat families were upregulated only in the double mutants (Fig. S2C). Interestingly, GO term analysis of genes upregulated only in the double mutants enriched most prominently for histone genes (Fig. S2D-E). Taken together, the data show that MET-2 and HPL-2 act redundantly to silence a subset of genes and repeats, suggesting MET-2 and HPL-2 function in independent pathways to silence some genes but synergize to silence others.

HPL-2 subnuclear foci are reinforced, but largely independent of H3K9me

Since our transcriptional data suggested an H3K9me-independent function of HPL-2, we tested whether HPL-2 foci are in any way dependent on H9K9me. In *met-2Δ set-25Δ* double mutant embryos lacking all H3K9me, HPL-2 still formed foci (Fig. 3A). Therefore, H3K9me is not necessary for HPL-2 foci formation. This result was unexpected because existing models suggest H3K9me2/me3 binding would be a driving force in the local accumulation of HPL-2(9, 10). We therefore interrogated the properties of HPL-2 foci using automated image analysis in WT and H3K9me-deficient backgrounds. Despite HPL-2 retaining its foci-forming competence in the absence of H3K9me, foci were fewer in number (WT: mean 5.7+/- 0.6 and *met-2Δ set-25Δ*: mean 3.6 +/- 0.5 foci/nucleus; p-value: 0.017), had a reduced fluorescence intensity (WT: mean 4.6+/- 0.4 and *met-2Δ set-25Δ*: mean 2.9 +/- 0.3 a. u.; p-value: 0.0046), and were measurably smaller (WT: mean 29.0+/- 0.5 and *met-2Δ set-25Δ*: mean 24.7 +/- 0.6 voxel/foci; p-value: 0.0036) in *met-2Δ set-25Δ* double mutant embryos on average (Fig. 3B-D). These changes could not be attributed to less HPL-2 protein overall, as both fluorescence intensity and western immunoblotting showed no decrease of total HPL-2 protein signal in the absence of H3K9me (Fig. 3E-F). Therefore, HPL-2 form foci even in the absence of H3K9me, but H3K9me may promote foci stability and/or assembly. We also observed that HPL-2 foci accumulate at the nuclear periphery in WT embryos (Fig. 3G) (26). Consistent with previous studies of MET-2 foci and heterochromatin, HPL-2 foci shifted away from the periphery when H3K9me was lost in the *met-2Δ set-25Δ* mutants (26, 38-40). Therefore, HPL-2 foci are dependent on MET-2 and SET-25 for targeting to the nuclear periphery.

Given MET-2's non-catalytic activity in heterochromatin function, we sought to distinguish whether H3K9me or MET-2 itself was important for HPL-2 foci or lamina association using catalytically deficient mutant *met-2-CD*. Animals expressing *met-2-CD; set-25Δ* did not rescue HPL-2 foci robustness (Fig. 3B-F), indicating that H3K9me rather than MET-2 reinforces HPL-2 foci. Likewise, *met-2-CD* could not rescue the association of HPL-2 with the nuclear lamina (Fig. 3G), implicating H3K9me in targeting HPL-2 foci to the lamina. In the reverse experiment, deletion of *hpl-2* (*hpl*-2*Δ*) did not decrease MET-2::mNeonGreen foci number, intensity, size, or enrichment at the periphery (Fig. S3A-E). Therefore, H3K9me reinforces HPL-2 protein foci and localization, while MET-2 traffics independently of HPL-2.

HPL-2 defective in H3K9me-binding retains transcriptional repression and foci-forming competence

To test directly the role of methyl-lysine binding for HPL-2 foci formation, we disrupted HPL-2's ability to bind H3K9me. HP1 binds H3K9me2/3 via a three-amino acid aromatic cage in the chromodomain (Fig. 4A). We mutated two phenylalanines of the HPL-2 aromatic cage to alanine, F19A and F43A (Fig. 3A, HPL-2-FFAA). Analogous mutations in other chromodomain proteins have been shown to disrupt

H3K9me binding (39, 41). We confirmed that this HPL-2FFAA double point mutant showed strongly impaired interaction with H3K9me2/3 using an in vitro binding assay (Fig. S4A). Protein levels of mKate2-tagged strains were not decreased in the HPL-2-FFAA strain relative to WT, indicating that the mutation does not affect expression (Fig. S4B-C).

If HPL-2 indeed has H3K9me-independent functions in ensuring transcriptional silencing, then the *hpl-2-FFAA* mutant may maintain gene repression of at least a subset of genes mis-expressed in the *hpl-2* deletion mutant. We therefore performed transcriptome analysis comparing WT, *hpl*-2*Δ*, and *hpl-2-FFAA* early embryos. We found that genes desilenced in *hpl*-2*Δ* embryos remained largely repressed in *hpl-2-FFAA* animals (Fig. 4B-C, S4D; FC = 2, FDR = 0.05), indicating that HPL-2 can silence genes in an H3K9me-independent manner. Nevertheless, gene expression in *hpl-2-FFAA* and *hpl-2Δ* correlated (R = 0.64), suggesting that the repression was not complete. We conclude that HPL-2 possesses a silencing function that does not require binding H3K9me.

Despite its compromised ability to bind H3K9me, HPL-2-FFAA mKate2-tagged protein formed foci (Fig. 4D). Consistent with the properties of HPL-2 foci in the *met-2Δ set-25Δ* double mutant lacking all H3K9me, the number and average size of foci were decreased in HPL-2-FFAA relative to HPL-2-WT (Fig 4D-F). These results demonstrate a direct role for H3K9me-binding in reinforcing the assembly or stability of HPL-2 foci. In contrast, foci intensity and peripheral positioning showed only modest effects in HPL-2-FFAA mutants vs. WT embryos (Fig. 4D, S4E-F), suggesting that H3K9me may exert some effects on HPL-2 protein indirectly. Further, HPL-2-FFAA continued to colocalize with MET-2-WT and MET-2-CD (Fig. S4G), suggesting that HPL-2-FFAA foci are correctly targeted despite its H3K9me-binding deficiency.

Having uncoupled HPL-2 protein foci from H3K9me binding, we tested whether HPL-2-FFAA could perform known functions of HPL-2. We first compared the ability of *hpl-2Δ* and *hpl-2-ffaa* mutants to promote proper tissue differentiation. Both HPL-2 and MET-2 function in the development of the adult *C elegans* vulva (21). *hpl-2* and *met-2* are classified into the genetically defined category of SynMuvB genes, which are typically thought of as a single pathway. Single mutant animals develop a normal vulva. In the presence of an additional mutation in a SynMuvA gene, such as *lin-15A*, doubly mutant animals fail to restrict vulval development in the maturing epidermis, resulting in ectopic pseudovulvae, also known as a Multivulva phenotype (Muv). We crossed *hpl*-2*Δ* or *hpl-2-FFAA* animals into a *lin-15A* mutant background. As expected, *hpl*-2*Δ;lin-15A* animals showed a high incidence of multivulva (Fig. 4G). In contrast, *hpl*-2-*FFAA; lin-15A* animals showed normal vulva development. Similar to *hpl-2-FFAA* animals, catalytically deficient *met-2-CD; lin-15A* animals also developed normally, while *met-2Δ; lin-15A* animals displayed a highly penetrant multivulva phenotype (Fig. S4H).

These data show that both HPL-2 and MET-2 can preserve normal vulval development even when their H3K9me-related functions are compromised.

Animals with mutations in the SynMuvB heterochromatin genes are also known to ectopically express germline genes in somatic cells (42-45). We asked whether this soma-to-germline phenotype was H3K9me-dependent using an endogenous GFP-tagged P-granule protein PGL-1::GFP (32, 46). We imaged the heads of L4 larvae to avoid confounding autofluorescence in the gut and the normal PGL-1 signal in the germline. While deletions of either *met-2* or *hpl-2* lead to a several-fold increase in ectopic GFP expression in the heads, animals expressing *met-2-CD* or *hpl-2-FFAA* retained nearly complete repression of PGL-1 expression (Figs. 4H, S4I). Taken together, these results show that both HPL-2 and MET-2 have H3K9me-independent functions in foci formation, transcriptional repression and vulva cell fate.

Physical interaction with multivalent binding partners are essential for MET-2 and HPL-2 H3K9me independent functions

Because both HPL-2 and MET-2 exhibit H3K9me-independent functions, we examined how their interaction partners contribute to foci formation and function. MET-2 foci are dependent on physical interaction with the intrinsically disordered domain (IDR) protein LIN-65 (26, 27). In the absence of *lin-65*, MET-2 does not concentrate in the nucleus and does not form foci. Similarly, an overexpressed HPL-2 was reported to form foci dependent on the C2-H2 zinc finger-containing protein LIN-13 (29). LIN-65's IDRs and LIN-13's predicted 24 zinc fingers create the potential for higher order interactions. Such multivalent interactions have been observed to contribute to biomolecular condensates (47, 48), and indeed MET-2 foci possess some properties associated with condensates (26). We interrogated whether MET-2 and/or HPL-2 foci are dependent on either or both of their multivalent co-factors LIN-65 and/or LIN-13, respectively. Knockdown of *lin-65* dispersed MET-2 from the nucleus as expected; however, HPL-2 foci remained (Fig. 5A). Knockdown of *lin-13* depleted HPL-2 foci as previously reported but was dispensable for MET-2 foci formation (Fig. 5A). We conclude HPL-2 and MET-2 colocalize in foci independent of each other or the other's required cofactor, LIN-13 and LIN-65, respectively.

We asked how LIN-13 and LIN-65 contribute to HPL-2 and MET-2 function in cell fate. The catalytic and non-catalytic functions of MET-2 are dependent on LIN-65 (25). Conversely, we also observed that LIN-65::GFP was lost in *met-2Δ* nuclei (Fig. S5A). Adding an NLS-tag to the C-terminus of LIN-65::GFP did not rescue LIN-65 in a *met-2*-deficient background, suggesting that LIN-65 is degraded rather than delocalized (data not shown). In contrast, *met-2-CD* rescued LIN-65::GFP nuclear foci (Fig.

S5A, S5B). These results show that MET-2 and LIN-65 are mutually dependent for stable accumulation into nuclear foci, but independent of H3K9me. Like MET-2, deletion of *lin-65* shows a high penetrance multivulva phenotype in the *lin-15A* mutant context (Fig. S5C and (49)). While loss of *lin-65* disrupts H3K9me, MET-2 nuclear accumulation and foci formation, loss of MET-2's catalytic cofactor ARLE-14 disrupts H3K9me deposition and MET-2 chromatin association without disrupting MET-2 nuclear foci (25, 27). We found that vulval development was normal in *arle-14Δ;lin-15A* double mutant animals (Fig. S5C). These results are consistent with an H3K9me-independent mechanism for vulval development. Next, we tested whether nuclear localization in the absence of *lin-65* was sufficient for MET-2 to promote cell fate by expressing MET-2 with a nuclear localization sequence (NLS; (27)). It was previously shown that this NLS could maintain MET-2 nuclear enrichment in the absence of *lin-65*; however, neither nuclear foci nor H3K9me levels were rescued (25). Just like H3K9me levels, *NLS::met-2* was not sufficient for normal vulval development in the absence of *lin-65* (Fig. S5D). Fertility assays also showed no rescue of progeny numbers in the *lin-65Δ;NLS::met-2* double mutant animals (Fig. S5E). Taken together, these results suggest that LIN-65 is stabilized by interaction with MET-2 and has an essential role in cell fate, correlating with foci formation, that cannot be rescued by either MET-2 catalytic activity or MET-2 accumulation in the nucleus.

Next, we examined the interaction between HPL-2 and LIN-13. A previous report demonstrated that HPL-2 and LIN-13 directly bind each other in yeast two hybrid studies (29). We performed immunoprecipitation of HPL-2::mKate2::3xFLAG followed by mass spectrometry (IP-MS) to characterize HPL-2 interactions in embryo lysates. LIN-13 peptide intensities were indeed enriched in the HPL-2::mKate2 strain relative to the N2 untagged control (Fig. 5B). Consistent with a model of independent recruitment, HPL-2 pulldowns did not enrich for MET-2, nor did previous MET-2 pulldowns enrich for HPL-2 (data not shown and (25-27).

We characterized in greater detail how the physical interaction with LIN-13 contributes to HPL-2 function. The data above demonstrating that the HPL-2-FFAA mutant suffices for vulval development and transcriptional repression argues against an essential role for the chromodomain. In contrast, two-hybrid interaction studies suggest that the HPL-2 chromoshadow domain (CSD) suffices for binding LIN-13, which is also implicated in proper vulva specification (29, 50-52). To test which domains were necessary for HPL-2 function, we used CRISPR to delete HPL-2's chromodomain (aa 19-71, ΔCD) or the portion of the CSD shared between both short and long isoforms that contains the conserved residues necessary for binding the PXVXL motif (53) in the FFAA background (aa 112-151, ΔCSD) (Fig. 5C). To characterized these domain mutants, we examined the interaction with LIN-13 via immunoprecipitation of the HPL-2 mutants followed by mass spectrometry (IP-MS). While LIN-13 remained enriched in ΔCD mutants to a similar extent as WT, LIN-13 enrichment was lost in FFAAΔCSD

embryos (Fig. 5D). Therefore, the HPL-2 chromoshadow domain is necessary for interaction with LIN-13 in vivo. Consistent with these data, the HPL-2 signal enriched in foci was retained in embryos lacking the chromodomain but lost in ΔCSD embryos, confirming that LIN-13-dependent physical interaction mediated by the chromoshadow domain are necessary for foci formation (Fig. 5E, 5F).

We tested how HPL-2 domains interacted with *lin-15A* in specification of the vulva. *hpl-2ΔCD;lin-15A* animals showed a low penetrance multivulva phenotype (8.2%, Fig. 6A). It follows we cannot exclude a structural role for the chromodomain in this process. In contrast, animals lacking the chromoshadow domain showed highly penetrant defects in vulva development (90.9%, Fig. 6A). Finally, we used qRT-PCR to interrogate genes identified by RNAseq to be repressed by HPL-2. Deletion of the chromodomain showed only modest effects on transcription, while embryos lacking the chromoshadow domain exhibited greater desilencing of genes, similar in magnitude to embryos in which *hpl-2* is deleted (Fig. 6B). Therefore, we conclude the HPL-2 chromoshadow domain mediates interactions with its multivalent binding partner LIN-13 to drive foci formation, repress transcription, and promote proper tissue differentiation.

Discussion

Recent studies have shown that multiple histone-modifying enzymes retain function in the absence of their enzymatic activity, raising the question of how these proteins interact with the protein readers of histone modifications in the absence of enzymatic activity. We find that the reader HPL-2/HP1 and writer MET-2/SETDB1 function in parallel pathways to silence distinct groups of genes (Fig. 6C). They also act redundantly and/or additively to silence a second cohort of sequences. These activities depend on physical interactions with distinct multivalent binding partners, the zinc finger LIN-13 for HPL-2 and the intrinsically disordered LIN-65/ATF7IP for MET-2. Interactions with these cofactors are critical for gene repression, organogenesis and localization of HPL-2 and MET-2 within heterochromatic foci. H3K9me is not necessary for either factor to concentrate into foci, but does contribute to HPL-2 foci robustness and distribution. These protein-protein interactions may explain the minor role of H3K9me binding in HPL-2-mediated gene repression.

The histone code hypothesis argues that a combinatorial crosstalk between post-translational modifications of histones regulates chromatin function, including the selective expression of genes (54). In particular, the role of H3K9 methylation in silencing of genes and repetitive elements is well-established (19, 55-58). Nevertheless, increasing evidence is uncoupling PTM writer proteins from their histone marks in their regulation of transcription and development. In Drosophila, the histone acetyltransferases (HATs) CBP and Gcn5 are required for zygotic genome activation, yet can perform their essential role in development independent of its acetylation activity (59). In mammalian cells, p300 plays an important role in transcription coactivation, but chromatin interactions have been reported to be opposed by its HAT activity (60). Use of chemical inhibitors of HAT activity has strengthened the evidence for acetylation-independent functions of CBP (61). Among methyltransferases, mammalian MLL3 and MLL4 have been shown to promote enhancer activation independent of their H3K4 HMT activity (62). G9a can function in transcriptional repression independent of its H3K9 HMT activity by recruiting DNA methyltransferases (63, 64). We found that the catalytic-deficient MET-2-CD rescues or mitigates germline and somatic phenotypes, prevents hyperacetylation, and is sufficient to silence a subset of genes repressed by MET-2 (Fig. S4H-I, and (25)). Intriguingly, a subsequent study showed SETDB1 bearing the homologous C1243A catalytic deficient mutation as MET-2-CD rescues defects in stem cell pluripotency caused by simultaneous triple-deletion of HP1α/β/γ, arguing that a non-catalytic activity of MET-2/SETDB1 may be conserved (65). MET-2-CD stabilizes LIN-65/ATF7IP, and both proteins are required for cell fate restriction (Fig S5). These findings suggest that protein-protein interactions between chromatin modifiers and their cofactors are required for an additional layer of regulation beyond that mediated by PTMs.

PTM reader proteins can also demonstrate dynamic, higher-order protein behaviors that are enhanced by, but not dependent on, chromatin marks. It has been shown, for example, that histone acetylation reader BRD4 forms condensates via its IDR, but that biophysical properties of these foci are altered in the presence of acetylation (18, 66, 67). We show that HPL-2 need not bind to H3K9me to repress transcription or promote appropriate vulva cell lineage; rather, H3K9me contributes to robust HPL-2 gene repression and protein dynamics in vivo. Consistently, in flies H3K9me enhances, but is not required for, HP1a accumulation at promoters and pericentromeric regions (68, 69). In contrast, H3K9me is required for anchoring of HPL-2 foci to the periphery (Fig. 3G). HP1 proteins consist of a H3K9me-reader chromodomain, a flexible hinge region, and a chromoshadow domain that conveys homo- and heterodimerization with binding partners. In mammals, the chromoshadow domain leads to the recruitment of Suvar3-9 and Suv420H2, leading to more repressive H3K9me and H4K20me3, respectively (70, 71). Several CSD interactions with chromatin-associated factors have been reported, including CAF-1, a nucleosome chaperone, and KAP-1, which forms a complex with SETDB1 and also associates with KRAB zinc finger proteins (72-76) . We demonstrated the CSD is required for interaction between HPL-2 and LIN-13 in vivo, the concentration of HPL-2 into foci, and the specification of the mature vulva. In contrast, the chromodomain played only a minor role in cell fate, transcription, and protein foci dynamics.

Multiple mechanisms may underlie how multivalent interactions concentrate proteins into functional compartments. For example, it has been proposed that p300 acts as a scaffold, activating transcription by simultaneously recruiting multiple transcription factors (60). Intrinsically disordered domains of proteins (IDRs) are strongly implicated in higher-order protein condensation (77). IDRs are unstructured but have unique biochemical attributes including electrostatic charge and primary sequence that have been shown to control protein targeting and function (78, 79). Post translation modification of IDRs have also been shown to regulate their function. Phosphorylation of HP1α unstructured regions was demonstrated to enhance intermolecular self-interactions, lowering the barrier to phase separation in vitro (17, 80). Our data and others demonstrate that HP1 homolog HPL-2 forms foci in vivo not via H3K9me or self-interactions but by binding LIN-13, whose 24 zinc fingers and LIN-35/Rb binding motif may serve as a scaffold promoting HPL-2 multivalent protein-protein and protein-chromatin interactions (29). Analogously, MET-2/SETDB1 possesses an unstructured N-terminus that is not sufficient to establish and/or maintain foci; rather, MET-2, likely via its N-terminus, interacts with the disordered protein LIN-65/ATF7IP to be recruited into higher-order structures, methylate H3K9, and repress transcription (25-28, 81-83). Importantly, the interplay between HPL-2 and MET-2 with their respective putative multivalent cofactors do not only drive foci formation, but together they provide an additional layer of regulation essential for cell lineage restriction and the silencing of germline genes in the soma (42-45). LIN-13, MET-2, and HPL-2 have been suggested to

work together with other heterochromatin-associated proteins to prevent DNA damage and germline apoptosis (19). We find that MET-2 and HPL-2 colocalize in foci in a LIN-13 dependent manner. Dissecting to what extent multivalent protein-protein and protein-chromatin interactions contribute to PTM-independent regulation of transcription and tissue identity remains an important challenge worthy of subsequent investigation.

Materials and Methods

Strains and maintenance

Strains used for these studies are documented in Supplementary Table 1. "Some strains were provided by the CGC, which is funded by NIH Office of Research Infrastructure Programs (P40 OD010440)." Animals were cultured at 20°C unless otherwise indicated. Embryos were isolated either by dissection or by standard bleaching protocols. RNA interference (RNAi) knockdown of genes was achieved as previously described (84, 85). Synchronized L1 animals were fed HT115 E coli expressing double stranded RNA targeting the indicated gene on nematode growth media plus 1 mM IPTG and 100 µg/mL carbenicillin. RNAi targeting *lin-13* was a gift from Francesca Palladino (CNRS Lyon).

Transgenesis

Targeted substitutions and deletions were created in endogenous gene loci using CRISPR-Cas9 exactly as previously described (86). AltR Cas9 and tracrRNA (IDT) were used. AltR crRNAs were synthesized by IDT. Edit-specific crRNA sequences and Homology Directed Repair template sequences (IDT) are provided in Supplementary Table 2.

Live microscopy

Imaging was performed at 20°C. 2D DIC images were captured using a Zeiss Axio Zoom V16 and Zeiss Axiocam 503 mono camera with ZEN 2.6 blue edition software. Fluorescent 3D imaging were obtained using an Olympus IX83 microscope outfitted with a Yokogawa CSU-W1 confocal 50 µm spinning disk, and Hamamatsu ORCA-Fusion sCMOS camera. Images were deconvolved with the Huygens Remote Manager. Automated image segmentation analysis of nuclei and foci was performed with Knime (87).

Developmental phenotypes

Fertility assays: L4 animals grown at the indicated temperature were placed one (25°C) or three (26°C) animals per plate. Egglayers were transferred to fresh plates every 24 hr for the duration of egglaying, after which total progeny were counted.

SynMuv assays: Gravid adults were allowed to lay eggs for several hours, then removed. Laid eggs were allowed to mature to day 1 adults for 72 hr at 20°C, at which time animals were visually scored for the presence or absence of abnormal vulva development.

Immunoprecipitation-mass spectrometry (IP-MS)

Immunoprecipitations were performed as previously reported (26). All steps were performed on ice or 4°C. Briefly, mixed embryos isolated by bleaching from 100,000 day 1 adult animals were homogenized

in TAP buffer (150 mM NaCl, 20 mM Tris-HCl, pH 7.5, 0.5% NP-40, 1 mM EDTA, 10% glycerol, 2× cOmplete-EDTA-free protease inhibitors (Roche), 1× Deacetylase Inhibitor (Active Motif), and 1 mM DTT) using 0.5 mm Glass Globules (Roth) and a Fast Prep-24 homogenizer (MP Biomedicals). Lysates were sonicated in 14 cycles of 15 s on, 30 s off using a Bioruptor Plus (Diagenode). Lysates were cleared via centrifugation at 21,000g for 10 min at 4°C. Anti-FLAG-M2 magnetic beads (Sigma) pre-washed in TAP buffer were added to 5 mg protein lysate and rotated overnight at 4°C. Beads were washed in TAP buffer 4 x 15 min, then 3 times with MS wash buffer (20 mM Tris-HCl, pH 7.5, 150 mM NaCl) to remove detergents.

Resin was resuspended in elution buffer (5% SDS, 10mM TCEP, 0.1 M TEAB), incubated for 10 min at 95°C and transferred into a new tube. Proteins were alkylated in 20 mM iodoacetamide for 30 min at 25°C and digested using S-Trap™ micro spin columns (Protifi) according to the manufacturer's instructions. Briefly, 12 % phosphoric acid was added to each sample (final concentration of phosphoric acid 1.2%) followed by the addition of S-trap buffer (90% methanol, 100 mM TEAB pH 7.1) at a ratio of 6:1. Samples were mixed by vortexing and loaded onto S-trap columns by centrifugation at 4000 g for 1 min followed by three washes with S-trap buffer. Digestion buffer (50 mM TEAB pH 8.0) containing sequencing-grade modified trypsin (1/25, w/w; Promega) was added to the S-trap column and incubate for 1h at 47 °C. Peptides were eluted by the consecutive addition and collection by centrifugation at 4000 g for 1 min of 40 ul digestion buffer, 40 µL of 0.2% formic acid and finally 35 µL 50% acetonitrile, 0.2% formic acid. Samples were dried using a Speedvac and stored at -20 °C until further use.

Dried peptides were resuspended in 0.1% aqueous formic acid and subjected to LC–MS/MS analysis using a Orbitrap Fusion Lumos Mass Spectrometer fitted with an EASY-nLC 1200 (Thermo Fisher Scientific) and a custom-made column heater set to 60°C. Peptides were resolved using a RP-HPLC column (75µm × 36cm) packed in-house with C18 resin (ReproSil-Pur C18–AQ, 1.9 µm resin; Dr. Maisch GmbH) at a flow rate of 0.2 µL/min. The following gradient was used for peptide separation: from 5% B to 12% B over 5 min to 35% B over 40 min to 50% B over 15 min to 95% B over 2 min followed by 18 min at 95% B. Buffer A was 0.1% formic acid in water and buffer B was 80% acetonitrile, 0.1% formic acid in water.

The mass spectrometer was operated in DDA mode with a cycle time of 3 seconds between master scans. Each master scan was acquired in the Orbitrap at a resolution of 120,000 FWHM (at 200 m/z) and a scan range from 375 to 1600 m/z followed by MS2 scans of the most intense precursors in the linear ion trap at "Rapid" scan rate with isolation width of the quadrupole set to 1.4 m/z. Maximum ion injection time was set to 50ms (MS1) and 35 ms (MS2) with an AGC target set to 1e6 and 1e4, respectively. Only peptides with charge state 2 – 5 were included in the analysis. Monoisotopic

precursor selection (MIPS) was set to Peptide, and the Intensity Threshold was set to 5e3. Peptides were fragmented by HCD (Higher-energy collisional dissociation) with collision energy set to 35%, and one microscan was acquired for each spectrum. The dynamic exclusion duration was set to 30s.

The acquired raw-files were searched using MSFragger (v. 4.0) implemented in FragPipe (v. 21.1) against a C. elegans database (consisting of 26584 protein sequences downloaded from Uniprot on 20220222) and 392 commonly observed contaminants spiked with the sequence of mKate2 using the "LFQ-MBR" workflow. Quantitative data was exported from FragPipe and analyzed using the MSstats R package v.4.13.0. (https://doi.org/10.1093/bioinformatics/btu305). Data was normalized, imputed using "AFT model-based imputation" and q-values for pairwise comparisons were calculated as implemented in MSstats.

in vitro binding assay

Embryo lysed in IVB buffer (30mM Tris-HCl pH 7.5, 600 mM NaCl, 1 mM EDTA pH 8.0, 5% glycerol, 1% Triton X-100, 2X cOmplete-EDTA-free protease inhibitors (Roche), and 1 mM DTT) (88) were processed exactly as in immunoprecitation above. Dynabeads™ MyOne™ Streptavidin C1 (Invitrogen) were rotated with 4X excess biotinylated H3 tail peptides (Anaspec) in TAP buffer for 4 hr at 4°C. Beads were then washed 3X in IVB buffer and stored on ice prior to use. Equivalent amounts of protein were distributed to tubes containing peptide-bead complexes and rotated overnight at 4°C. Beads were washed 4X with IVB buffer, then resuspended in TAP buffer and stored at -20°C until use.

Western

10 µg of total protein from embryo lysates was separated on Criterion XT Bis-Tris gels (Bio-Rad) using either MES or MOPS buffer (Invitrogen). Proteins were transferred using a Trans-blot semi-dry system and Trans-blot Turbo Midi 0.2 µm PVDF pre-cut membranes (Bio-Rad). Membranes were blocked in either PBS + 0.5% Tween-20 (PBST) containing 5% milk (Sigma) or Protein-free blocking buffer (Pierce) depending on the antibody of interest. Primary antibodies include 1:10,000 mouse anti-H3K9ac and 1:10,000 mouse anti-H3K27ac (gifts of H. Kimura), 1:10,000 rabbit anti-H2B (Abcam ab1790), and 1:25,000-1:50,000 mouse anti-FLAG M2 conjugated to HRP (Sigma). Blots were rotated overnight at 4°C, washed three times in PBST, blocked again and exposed to HRP-conjugated secondary antibodies, when applicable, for 1 h at RT. Secondary antibodies include 1:100,000 goat anti-mouse IgG HRP (Jackson ImmunoResearch 115-035-146) or 1:100,000 goat rabbit IgG HRP (Jackson ImmunoResearch 111-035-144). We used Immobilon HRP substrate (Millipore) and detected signal using a Fusion FX camera operated with Fusion FX7 Edge Software (Vilber).

RNA isolation

RNA was extracted from early embryos from synchronized cultures grown at 20°C as reported previously using Trizol (Invitrogen) (24). For in *met-2Δ hpl-2Δ* double mutant embryos, heterozygotes with a GFP + balancer were expanded. Non-fluorescent L1 progeny—maternally rescued, homozygous double mutant animals—were selected using a COPAS Biosort (Union Biometrica), from which early embryos were harvested. Embryos were freeze cracked five times, then RNA was extracted with choloroform followed by isopropanol precipitation. Further purification was performed with the RNA Clean and Concentrator kit (Zymo).

qPCR

cDNA was synthesized using Maxima H Minus Reverse Transcriptase (ThermoFisher) according to manufacturer's instructions. 1 ug RNA was primed using Oligo(dT)20 primer (Invitrogen). Reactions were performed using the PowerUp SYBR Green Master Mix (Applied Biosystems). Ct values were determined with Mastercycler EP realplex software. Housekeeping gene pmp-3 was used for normalization (89) and relative expression was calculated with the ΔΔCt method (90).

RNA sequencing

Libraries were produced using the Stranded Total RNA Prep Ligation with Ribo-Zero Plus Kit (Illumina). rRNA was depleted using the Ribo-Zero Plus kit supplemented with custom made C. elegans specific rDNA oligos (IDT). Libraries were profiled in a DNA 1000 Chip on a 2100 Bioanalyser (Agilent technologies) and quantified using the Qubit 1x dsDNA HS Assay Kit, in a Qubit 4.0 Fluorometer (Life technologies). Equimolar amounts of indexed libraries were pooled and sequenced on a NextSeq 2000 (Illumina). Reads were analysed as described previously (25). Adapter were trimmed using Trimmomatic v0.39. Reads were aligned to the C. elegans genome (ce10) with the R package QuasR v1.44.0, (www.bioconductor.org/packages/2.12/bioc/html/QuasR.html). The command "proj <- qAlign("samples.txt","BSgenome. Celegans.UCSC.ce10", splicedAlignment=TRUE)" instructs hisat296 to align using default parameters, considering unique reads for genes and genome wide distribution. Count Tables of reads mapping within annotated exons in WormBase (WS220) were constructed using the qCount function of the QuasR package to quantify the number of reads in each window (qCount(proj, GRange_object, orientation="same")) and normalized by division by the total number of reads in each library and multiplied by the average library size. Transformation into log2 space was performed after the addition of a pseudocount of 12 to minimize large changes in abundance fold change (FC) caused by low count numbers. The EdgeR package v4.2 was applied to select genes with differential transcript abundances between indicated genotypes (contrasts) based on false discovery rates (FDR) for genes (FDR <0.05 and log2 fold change >1 for up regulated genes and <-1 for down regulated genes). Replica correlations are shown in Fig SXXX of GO-Terms were extracted from

wormbase.org and the GO-Term and KEGG pathway enrichment analysis was performed using the gprofiler2 package (v 0.2.3) as an interface to g: Profiler (91).

Acknowledgements

We would like to thank: the Imaging Core facility (IMCF), the Proteomics core facility members (Biozentrum, University of Basel) and the Genomics Core Facility (IMB, Mainz) for helpful discussions and technical assistance; and Iskra Katic at Fredrich Miescher Institute (FMI) for providing sound advice and technical support for fluidic sorting of animals. Jan Padeken is associated with the SFB 1551 Project No. 464588647 of the DFG (Deutsche Forschungsgemeinschaft).

Authors' Contributions.

CED: Conceived the project, performed experiments, data curation, formal analysis, methodology, Investigation: data in figures , Writing: original draft, review, editing.

JEY: Investigation: performed experiments

SG: Funding acquisition

JP: Investigation: data in figures; Writing: review, editing; funding acquisition

SEM: conceptualization; Writing: review, editing, supervision; funding acquisition, project administration

Availability of data and materials

Figure Legends

Fig. 1. MET-2 and HPL-2 colocalize via independent recruitment into heterochromatic foci. (**A**) Schematic of HPL-2 protein isoforms expressed from the same locus, with isoform percentage of total protein indicated in parentheses as determined by Western blot (mean, N = 3; see also Fig. 3F, S4B). Red triangle = mKate2::3xFLAG insertion site in the hinge domain. (**B**) Representative images of MET-2::mNeonGreen co-expressed with HPL-2::mKate2. Dashed oval indicates the circumference of the embryo. Dashed boxes indicate example nuclei enlarged below. Scale bar, 5 µm. N = 3, n = 30. **(C)** Representative images of embryos co-expressing MET-2::mNeonGreen with HPL-2::mKate2 treated with *met-2*, or *hpl-2* RNAi or empty vector control. Scale bar, 5 µm. N = 3, n = 30. **(D)** Representative images of MET-2::mNeonGreen co-expressed with HPL-2::mKate2 in WT, *met-2-CD*, and *hpl-2-FFAA* backgrounds. Scale bar, 5 µm. N = 3, n = 30. **(E)** Mean progeny per worm at 26°C in WT, *hpl-2Δ*, and *hpl-2::mKate2::3xFLAG*. N = 2, n = 60 egg layers. Bars indicate mean value of each genotype.

Fig. S1. MET-2 and HPL-2 foci formation is independent of associated genes implicated in heterochromatin. (**A**) Representative images of embryos co-expressing MET-2::mNeonGreen with HPL-2::mKate2 treated with the indicated RNAi or empty vector control. Scale bar, 5 µm. N = 3, n = 30. (**B**) Representative images of embryos expressing either HPL-1::mKate2 or HPL-2::mKate2. Dashed oval indicates the circumference of the embryo. Inset shows overexposed region highlighted in the dashed box. Scale bar, 5 µm. N = 3, n = 75.

Fig 2. H3K9me and HPL-2 act independently to repress transcription. (**A**) Representative images and quantification of GFP signal from the *gwIs4* heterochromatic array. N = 3, n(embryos): WT vector = 99, WT *hpl-2* RNAi = 134, *met-2Δ set-25Δ* vector = 39, *met-2Δ set-25Δ hpl-2* RNAi = 53. *$p < 3x10^{-4}$, **$p < 10^{-9}$ by one-way ANOVA, followed by Bonferroni post hoc test. (**B**) Representative images of vulva development in adult animals. Normal vulvae = circle, multivulva defects = arrowheads. Quantification reported previously (21). (**C**) Venn diagram showing overlap of *hpl-2Δ* and *met-2Δ*-derepressed genes measured by RNAseq. N = 3, FC > 2, FDR < 0.05. (**D**) Representative western blot and quantification of acetylated H3K9 normalized to histone H2B in WT, *hpl-2Δ* and *met-2Δ* single mutants. *N* = 4. *p = 0.034 by two-sided *t*-test. (**E**) Representative western blot and quantification of H3K27 acetylation normalized to histone H2B in WT, *hpl-2Δ* and *met-2Δ* single mutants. *N* = 3. *p = 0.014 by two-sided *t*-test. (**F**) Venn diagram and (**G**) heat map showing up-regulated genes in *met-2Δ hpl-2Δ* double mutant early embryos measured by RNAseq, and the subset of genes independently observed to be de-repressed in *hpl-2Δ* and/or *met-2Δ* single mutant early embryos. N = 3, FC > 2, FDR < 0.05. (**H**) qRT-PCR of a subset of *met-2Δ hpl-2Δ* double mutant up-regulated genes or the control gene *lmn-1*. Bars show means while dots indicate individual measurements. N = 3.

Fig S2. MET-2 and HPL-2 employ redundant mechanisms to silence genes and repeats. Venn diagrams showing overlap of *set-25Δ* mutant upregulated genes with (**A**) *hpl-2Δ* mutant or (**B**) *met-2Δ* mutants upregulated genes measured in independent RNAseq experiments. N = 3, FC > 2, FDR < 0.05. (**C**) Heat map showing *met-2Δ hpl-2Δ* up-regulated repeat families measured by RNAseq, and the subset of genes independently observed de-repressed in *met-2Δ* early embryos. N = 3, FC > 2, FDR < 0.05. (**D**) GO Terms from *met-2Δ hpl-2Δ* RNAseq. (**D**) Heat map showing *met-2Δ hpl-2Δ* up-regulated histone genes, as in (C).

Fig 3. HPL-2 forms nuclear foci independent of H3K9 methylation. (**A**) Representative live images of HPL-2::mKate2::3xFLAG in WT, *met-2Δ set-25Δ*, or *met-2-CD set-25Δ* embryos. Scale bar, 5 µm. N = 3, n = 30. Quantification of HPL-2::mKate2 foci from (A) measuring (**B**) foci number per nucleus, (**C**) size of foci, (**D**) mean foci intensity per nucleus, and (**E**) mean nuclear intensity. (**F**) Representative western blot of HPL-2::mKate2::3xFLAG protein levels in WT, *met-2Δ set-25Δ*, or *met-2-CD set-25Δ* embryos. N = 4. (**G**) Quantification of HPL-2::mKate2 foci distance to the nuclear periphery. *P-values (*met-2Δ set-25Δ* , *met-2-CD set-25Δ* vs WT): (B) $p = 0.017$, $p = 6.0 \times 10^{-3}$, (C) $p = 4.2 \times 10^{-3}$, $p < 3.6 \times 10^{-3}$, (D) $p = 3.1 \times 10^{-4}$, $p = 4.6 \times 10^{-3}$, (E) not significant, (G) $p = 2.1 \times 10^{-13}$, $p < 2.2 \times 10^{-16}$, by one-way ANOVA, followed by Tukey post hoc test.

Fig S3. MET-2 foci are independent of *hpl-2*.(**A**) Representative live images of MET-2::mNeonGreen in WT and *hpl-2Δ* embryos. Scale bar, 5 µm. N = 3, n = 30. Quantification of MET-2::mNeonGreen foci (**B**) number, (**C**) intensity, (**D**) size, and (**E**) distance to the nuclear periphery from data in (A). *P-values (*hpl-2Δ* vs WT): (B) not significant (NS), (C) NS (D) $p = 0.011$, (E) NS using by one-way ANOVA, followed by Tukey post hoc test.

Fig 4. HPL-2 defective in binding H3K9me2/3 suffices for foci formation and cell identity. (**A**) Schematic of the HPL-2 aromatic cage (F19, W41, F43) (53, 92), and the *hpl-2-FFAA* double point mutation. (**B**) RNAseq scatterplot and gene heat map (**C**) comparing gene expression between *hpl-2Δ* and *hpl-2-FFAA* mutant embryos. N = 3, FC > 2, FDR < 0.05 (**D**) Representative live images of HPL-2::mKate2::3xFLAG in WT or *hpl-2-FFAA* embryos. Scale bar, 5 µm. N = 3, n = 30. Quantification of HPL-2::mKate2 foci (**E**) number and (**F**) size from data in (D). N = 3. *P-values (*hpl-2-FFAA* vs *hpl-2-WT*): (E) $p = 2.8 \times 10^{-3}$, (F) $p = 2.8 \times 10^{-3}$ by one-way ANOVA, followed by Tukey post hoc test. (**G**) Representative DIC live images and quantification of multivulva (Muv) defects in worms expressing *hpl-2-WT*, *hpl-2Δ* or *hpl-2-FFAA* in the sensitized *lin-15A(n767)* background. Normal vulvae = circle, multivulva defects = arrowheads. N = 3. n: WT = 1437, *hpl-2Δ* = 1975, *hpl-2-FFAA* = 1483. (**H**) Representative live image maximum projections and signal quantification of endogenously-tagged PGL-1::GFP in the heads of L4 animals. Body is outlined in dashed line; mouth is to the right. Arrowhead = faint ectopic expression.

Scale bar = 10 µm, N = 3, n = 30. *p < 10^{-5}, ns = not significant by one-way ANOVA, followed by Tukey post hoc test.

Fig S4. H3K9me deposition is not required for vulva specification. (**A**) Representative Western blot of H3K9me peptide in vitro binding assay. Mean +/- standard error ratio of FFAA / WT bands for each peptide is shown above the blot. N = 3. *p = 1.8 x 10^{-4}, **p = 2.6 x 10^{-4} by two-sided T test. (**B**) Representative western blot of HPL-2::mKate2::3xFLAG in *hpl-2-WT* vs. *hpl-2-FFAA* protein levels. N = 4. (**C**) Image quantification in *hpl-2-WT* vs. *hpl-2-FFAA* of HPL-2::mKate2::3xFLAG nuclear intensity from Fig. 2D, p = 4.1 x 10^{-3} by one-way ANOVA, followed by Tukey post hoc test. (**D**) Venn diagram showing overlap of *hpl-2Δ* and *hpl-2-FFAA*-derepressed genes measured by RNAseq. N = 3, FC > 2, FDR < 0.05 Image quantification in *hpl-2-WT* vs. *hpl-2-FFAA* of HPL-2::mKate2::3xFLAG (**E**) foci intensity, and (**F**) distance to the nuclear periphery from Fig. 3D. P-values (*hpl-2-FFAA* vs *hpl-2-WT*): (E) not significant, (F) p = 0.039 by one-way ANOVA, followed by Tukey post hoc test. (**G**) Representative images of MET-2::mNeonGreen co-expressed with HPL-2::mKate2 in WT, *met-2-CD*, and *hpl-2-FFAA* backgrounds. Scale bar, 5 µm. N = 3, n = 30. (**H**) Representative DIC live images and quantification of multivulva (Muv) defects in worms expressing *met-2-WT*, *met-2Δ* or *met-2-CD* in the sensitized *lin-15A(n767)* background. Normal vulvae = circle, multivulva defects = arrowheads. N = 3. n: WT = 1463, *met-2Δ* = 1141, *met-2-cd* = 1346. (**I**) Representative live image maximum projections and signal quantification of endogenously-tagged PGL-1::GFP in the heads of L4 animals. Body is outlined in dashed line; mouth is to the right. Arrowhead = faint ectopic expression. Scale bar = 10 µm, N = 3, n = 30. *p < 10^{-5}, ns = not significant by one-way ANOVA, followed by Tukey post hoc test.

Fig. 5. HPL-2 physical interactions via its chromoshadow domain promote foci formation. (**A**) Representative images of embryos co-expressing MET-2::mNeonGreen with HPL-2::mKate2 treated with the indicated RNAi or empty vector control. Scale bar, 5 µm. N = 3, n = 30. (**B**) anti-FLAG immunoprecipitation coupled to mass spectrometry enrichment of mKate2 and LIN-13 in untagged and HPL-2::mKate2::3xFLAG embryos. N = 3. (**C**) Schematic of chromodomain (ΔCD) or chromoshadow domain (ΔCSD) deletions created in HPL-2::mKate2 expressing animals (WT or FFAA, respectively). Positions of first and last amino acids of the deletions, replaced with Gly-Ser-Gly, are indicated. For clarity, only the short isoform is shown. (**D**) LIN-13 spectral intensity normalized to that of mKate2 in WT, *hpl-2-ΔCD*, and *hpl-2-FFAAΔCSD*. N = 3. *p = 4 x 10^{-6}, ns = not significant by two-sided T test. (**E**) Representative live images of HPL-2::mKate2 in WT, HPL-2-ΔCD, and HPL-2-FFAAΔCSD embryos. Scale bar, 5 µm. N = 3, n = 30. (**F**) Quantification of foci intensity relative to nuclear signal from (E). HPL-2ΔCD vs WT not significant, HPL-2-FFAAΔCSD vs WT p < 2.2 x 10^{-16} using one-way ANOVA, followed by Tukey post hoc test.

Fig. S5. Interaction with LIN-65 is essential for MET-2 function specifying the vulva. (A) Representative live images of endogenously tagged LIN-65::GFP in WT, *met-2Δ*, and *met-2-CD* embryos. Scale bar, 5 µm. N = 3, n = 45. Dashed lines indicate embryo circumference. (**B**) Quantification of foci number from (A). n.d. = not detected, met-2-CD vs WT p = 0.028 using two-sided Wilcoxon signed-rank test. (**C**) Quantification of multivulva (Muv) defects in *lin-65Δ* or *arle-14Δ* mutants in the sensitized *lin-15A(n767)* background. N = 3. n: *lin-15A* = 1159, *lin-65Δ;lin-15A* = 1199, *arle-14Δ;lin-15A* = 903. (**D**) Quantification of multivulva (Muv) defects in worms expressing an endogenously tagged nuclear localized NLS::met-2 in the presence or absence of *lin-65* and *lin-15A*. N = 3. n: WT = 429, *lin-15A* = 404, *lin-65Δ* = 434, *NLS::met-2* = 548, *lin-65Δ;NLS::met-2* = 467, *lin-65Δ;lin-15A* = 650, *NLS::met-2;lin-15A* = 589, *lin-65Δ;NLS::met-2;lin-15A* = 692 . (**E**) Progeny number per worm 25°C in WT, *lin-65Δ*, NLS::met-2, and *lin-65Δ;NLS::met-2*. *N* = 3, n = 45 egglayers. *$p < 10^{-5}$, ns = not significant by by one-way ANOVA, followed by Tukey post hoc test.

Figure 6. HPL-2 chromoshadow domain is essential for cell fate acquisition

(**A**) Quantification of multivulva (Muv) defects in worms expressing, *hpl-2Δ* or mKate2-tagged strains shown in (A) in the sensitized *lin-15A(n767)* background. N = 3. n: *hpl-2Δ* = 859, WT = 899, *hpl-2-ΔCD* = 887, *hpl-2-FFAAΔCSD* = 941. (**B**) qRT-PCR of a subset of *hpl-2Δ* up-regulated genes or the control gene *lmn-1* in *hpl-2Δ* or mKate2-tagged strains shown in (A). Bars show means while dots indicate individual measurements. N = 3. (**C**) Model: Interactions with multivalent cofactors are necessary for H3K9me-indpendent functions of HPL-2 and MET-2 during development. CSD-dependent protein-protein interactions with LIN-13 recruits HPL-2 into foci and suffices to restrict cell fate and repress transcription while MET-2 catalytic and non-catalytic activities require the intrinsically disordered domain protein LIN-65.

References

1. J. Padeken, P. Heun, Nucleolus and nuclear periphery: velcro for heterochromatin. *Curr Opin Cell Biol* **28**, 54-60 (2014).
2. J. Padeken, S. P. Methot, S. M. Gasser, Establishment of H3K9-methylated heterochromatin and its functions in tissue differentiation and maintenance. *Nat Rev Mol Cell Biol* **23**, 623-640 (2022).
3. M. W. Chen *et al.*, H3K9 histone methyltransferase G9a promotes lung cancer invasion and metastasis by silencing the cell adhesion molecule Ep-CAM. *Cancer Res* **70**, 7830-7840 (2010).
4. G. K. Griffin *et al.*, Epigenetic silencing by SETDB1 suppresses tumour intrinsic immunogenicity. *Nature* **595**, 309-314 (2021).
5. A. V. Karanth *et al.*, Emerging role of SETDB1 as a therapeutic target. *Expert Opin Ther Targets* **21**, 319-331 (2017).
6. D. Nicetto *et al.*, H3K9me3-heterochromatin loss at protein-coding genes enables developmental lineage specification. *Science* **363**, 294-297 (2019).
7. S. Prashanth, R. Radha Maniswami, G. Rajajeyabalachandran, S. K. Jegatheesan, SETDB1, an H3K9-specific methyltransferase: An attractive epigenetic target to combat cancer. *Drug Discov Today* **29**, 103982 (2024).
8. W. Zhang *et al.*, Aging stem cells. A Werner syndrome stem cell model unveils heterochromatin alterations as a driver of human aging. *Science* **348**, 1160-1163 (2015).
9. A. Kumar, H. Kono, Heterochromatin protein 1 (HP1): interactions with itself and chromatin components. *Biophys Rev* **12**, 387-400 (2020).
10. J. M. Schoelz, N. C. Riddle, Functions of HP1 proteins in transcriptional regulation. *Epigenetics Chromatin* **15**, 14 (2022).
11. D. Canzio *et al.*, A conformational switch in HP1 releases auto-inhibition to drive heterochromatin assembly. *Nature* **496**, 377-381 (2013).
12. C. Keller *et al.*, HP1(Swi6) mediates the recognition and destruction of heterochromatic RNA transcripts. *Mol Cell* **47**, 215-227 (2012).
13. R. R. Meehan, C. F. Kao, S. Pennings, HP1 binding to native chromatin in vitro is determined by the hinge region and not by the chromodomain. *EMBO J* **22**, 3164-3174 (2003).
14. C. Muchardt *et al.*, Coordinated methyl and RNA binding is required for heterochromatin localization of mammalian HP1alpha. *EMBO Rep* **3**, 975-981 (2002).
15. S. Biswas *et al.*, HP1 oligomerization compensates for low-affinity H3K9me recognition and provides a tunable mechanism for heterochromatin-specific localization. *Sci Adv* **8**, eabk0793 (2022).
16. F. Erdel *et al.*, Mouse Heterochromatin Adopts Digital Compaction States without Showing Hallmarks of HP1-Driven Liquid-Liquid Phase Separation. *Mol Cell* **78**, 236-249 e237 (2020).
17. A. G. Larson *et al.*, Liquid droplet formation by HP1alpha suggests a role for phase separation in heterochromatin. *Nature* **547**, 236-240 (2017).
18. A. R. Strom *et al.*, Interplay of condensation and chromatin binding underlies BRD4 targeting. *Mol Biol Cell* **35**, ar88 (2024).
19. A. N. McMurchy *et al.*, Correction: A team of heterochromatin factors collaborates with small RNA pathways to combat repetitive elements and germline stress. *Elife* **6** (2017).
20. J. M. Garrigues, S. Sidoli, B. A. Garcia, S. Strome, Defining heterochromatin in C. elegans through genome-wide analysis of the heterochromatin protein 1 homolog HPL-2. *Genome Res* **25**, 76-88 (2015).
21. E. C. Andersen, H. R. Horvitz, Two C. elegans histone methyltransferases repress lin-3 EGF transcription to inhibit vulval development. *Development* **134**, 2991-2999 (2007).
22. T. Simonet, R. Dulermo, S. Schott, F. Palladino, Antagonistic functions of SET-2/SET1 and HPL/HP1 proteins in C. elegans development. *Dev Biol* **312**, 367-383 (2007).
23. J. Padeken *et al.*, Synergistic lethality between BRCA1 and H3K9me2 loss reflects satellite derepression. *Genes Dev* **33**, 436-451 (2019).

24. P. Zeller *et al.*, Histone H3K9 methylation is dispensable for Caenorhabditis elegans development but suppresses RNA:DNA hybrid-associated repeat instability. *Nat Genet* **48**, 1385-1395 (2016).
25. C. E. Delaney *et al.*, SETDB1-like MET-2 promotes transcriptional silencing and development independently of its H3K9me-associated catalytic activity. *Nat Struct Mol Biol* **29**, 85-96 (2022).
26. C. E. Delaney *et al.*, Heterochromatic foci and transcriptional repression by an unstructured MET-2/SETDB1 co-factor LIN-65. *J Cell Biol* **218**, 820-838 (2019).
27. B. Mutlu *et al.*, Regulated nuclear accumulation of a histone methyltransferase times the onset of heterochromatin formation in C. elegans embryos. *Sci Adv* **4**, eaat6224 (2018).
28. T. Tsusaka, C. Shimura, Y. Shinkai, ATF7IP regulates SETDB1 nuclear localization and increases its ubiquitination. *EMBO Rep* **20**, e48297 (2019).
29. V. Coustham *et al.*, The C. elegans HP1 homologue HPL-2 and the LIN-13 zinc finger protein form a complex implicated in vulval development. *Dev Biol* **297**, 308-322 (2006).
30. T. Patel, O. Hobert, Coordinated control of terminal differentiation and restriction of cellular plasticity. *Elife* **6** (2017).
31. F. Couteau, F. Guerry, F. Muller, F. Palladino, A heterochromatin protein 1 homologue in Caenorhabditis elegans acts in germline and vulval development. *EMBO Rep* **3**, 235-241 (2002).
32. S. P. Methot *et al.*, H3K9me selectively blocks transcription factor activity and ensures differentiated tissue integrity. *Nature cell biology* **23**, 1163-1175 (2021).
33. R. F. Ketting, T. H. Haverkamp, H. G. van Luenen, R. H. Plasterk, Mut-7 of C. elegans, required for transposon silencing and RNA interference, is a homolog of Werner syndrome helicase and RNaseD. *Cell* **99**, 133-141 (1999).
34. E. M. Maine *et al.*, EGO-1, a putative RNA-dependent RNA polymerase, is required for heterochromatin assembly on unpaired dna during C. elegans meiosis. *Curr Biol* **15**, 1972-1978 (2005).
35. N. E. Weiser *et al.*, MORC-1 Integrates Nuclear RNAi and Transgenerational Chromatin Architecture to Promote Germline Immortality. *Dev Cell* **41**, 408-423 e407 (2017).
36. J. Padeken *et al.*, Argonaute NRDE-3 and MBT domain protein LIN-61 redundantly recruit an H3K9me3 HMT to prevent embryonic lethality and transposon expression. *Genes Dev* **35**, 82-101 (2021).
37. P. Meister, B. D. Towbin, B. L. Pike, A. Ponti, S. M. Gasser, The spatial dynamics of tissue-specific promoters during C. elegans development. *Genes Dev* **24**, 766-782 (2010).
38. B. D. Towbin *et al.*, Step-wise methylation of histone H3K9 positions heterochromatin at the nuclear periphery. *Cell* **150**, 934-947 (2012).
39. A. Gonzalez-Sandoval *et al.*, Perinuclear Anchoring of H3K9-Methylated Chromatin Stabilizes Induced Cell Fate in C. elegans Embryos. *Cell* **163**, 1333-1347 (2015).
40. A. Poleshko *et al.*, H3K9me2 orchestrates inheritance of spatial positioning of peripheral heterochromatin through mitosis. *Elife* **8** (2019).
41. S. A. Jacobs, S. Khorasanizadeh, Structure of HP1 chromodomain bound to a lysine 9-methylated histone H3 tail. *Science* **295**, 2080-2083 (2002).
42. A. K. Knutson, A. Rechtsteiner, S. Strome, Reevaluation of whether a soma-to-germ-line transformation extends lifespan in Caenorhabditis elegans. *Proc Natl Acad Sci U S A* **113**, 3591-3596 (2016).
43. L. N. Petrella *et al.*, synMuv B proteins antagonize germline fate in the intestine and ensure C. elegans survival. *Development* **138**, 1069-1079 (2011).
44. A. M. Saffer, D. H. Kim, A. van Oudenaarden, H. R. Horvitz, The Caenorhabditis elegans synthetic multivulva genes prevent ras pathway activation by tightly repressing global ectopic expression of lin-3 EGF. *PLoS Genet* **7**, e1002418 (2011).
45. X. Wu, Z. Shi, M. Cui, M. Han, G. Ruvkun, Repression of germline RNAi pathways in somatic cells by retinoblastoma pathway chromatin complexes. *PLoS Genet* **8**, e1002542 (2012).
46. A. Putnam, M. Cassani, J. Smith, G. Seydoux, A gel phase promotes condensation of liquid P granules in Caenorhabditis elegans embryos. *Nat Struct Mol Biol* **26**, 220-226 (2019).

47. S. Maharana *et al.*, RNA buffers the phase separation behavior of prion-like RNA binding proteins. *Science* **360**, 918-921 (2018).
48. P. Mohanty *et al.*, Principles Governing the Phase Separation of Multidomain Proteins. *Biochemistry* **61**, 2443-2455 (2022).
49. C. J. Ceol, F. Stegmeier, M. M. Harrison, H. R. Horvitz, Identification and classification of genes that act antagonistically to let-60 Ras signaling in Caenorhabditis elegans vulval development. *Genetics* **173**, 709-726 (2006).
50. E. L. Ferguson, H. R. Horvitz, The multivulva phenotype of certain Caenorhabditis elegans mutants results from defects in two functionally redundant pathways. *Genetics* **123**, 109-121 (1989).
51. A. Melendez, I. Greenwald, Caenorhabditis elegans lin-13, a member of the LIN-35 Rb class of genes involved in vulval development, encodes a protein with zinc fingers and an LXCXE motif. *Genetics* **155**, 1127-1137 (2000).
52. J. H. Thomas, C. J. Ceol, H. T. Schwartz, H. R. Horvitz, New genes that interact with lin-35 Rb to negatively regulate the let-60 ras pathway in Caenorhabditis elegans. *Genetics* **164**, 135-151 (2003).
53. A. Thiru *et al.*, Structural basis of HP1/PXVXL motif peptide interactions and HP1 localisation to heterochromatin. *EMBO J* **23**, 489-499 (2004).
54. T. Jenuwein, C. D. Allis, Translating the histone code. *Science* **293**, 1074-1080 (2001).
55. A. Bulut-Karslioglu *et al.*, Suv39h-dependent H3K9me3 marks intact retrotransposons and silences LINE elements in mouse embryonic stem cells. *Mol Cell* **55**, 277-290 (2014).
56. J. C. Peng, G. H. Karpen, H3K9 methylation and RNA interference regulate nucleolar organization and repeated DNA stability. *Nature cell biology* **9**, 25-35 (2007).
57. A. H. Peters *et al.*, Loss of the Suv39h histone methyltransferases impairs mammalian heterochromatin and genome stability. *Cell* **107**, 323-337 (2001).
58. A. V. Probst *et al.*, A strand-specific burst in transcription of pericentric satellites is required for chromocenter formation and early mouse development. *Dev Cell* **19**, 625-638 (2010).
59. F. Ciabrelli *et al.*, CBP and Gcn5 drive zygotic genome activation independently of their catalytic activity. *Sci Adv* **9**, eadf2687 (2023).
60. J. J. Ferrie *et al.*, p300 is an obligate integrator of combinatorial transcription factor inputs. *Mol Cell* **84**, 234-243 e234 (2024).
61. G. Hunt, A. Boija, M. Mannervik, p300/CBP sustains Polycomb silencing by non-enzymatic functions. *Mol Cell* **82**, 3580-3597 e3589 (2022).
62. K. M. Dorighi *et al.*, Mll3 and Mll4 Facilitate Enhancer RNA Synthesis and Transcription from Promoters Independently of H3K4 Monomethylation. *Mol Cell* **66**, 568-576 e564 (2017).
63. Q. Jiang *et al.*, G9a Plays Distinct Roles in Maintaining DNA Methylation, Retrotransposon Silencing, and Chromatin Looping. *Cell Rep* **33**, 108315 (2020).
64. M. Tachibana, Y. Matsumura, M. Fukuda, H. Kimura, Y. Shinkai, G9a/GLP complexes independently mediate H3K9 and DNA methylation to silence transcription. *EMBO J* **27**, 2681-2690 (2008).
65. L. Dong *et al.*, A functional crosstalk between the H3K9 methylation writers and their reader HP1 in safeguarding embryonic stem cell identity. *Stem Cell Reports* **18**, 1775-1792 (2023).
66. B. A. Gibson *et al.*, Organization of Chromatin by Intrinsic and Regulated Phase Separation. *Cell* **179**, 470-484 e421 (2019).
67. B. R. Sabari *et al.*, Coactivator condensation at super-enhancers links phase separation and gene control. *Science* **361** (2018).
68. N. Atinbayeva *et al.*, Inheritance of H3K9 methylation regulates genome architecture in Drosophila early embryos. *EMBO J* **43**, 2685-2714 (2024).
69. M. L. Figueiredo, P. Philip, P. Stenberg, J. Larsson, HP1a recruitment to promoters is independent of H3K9 methylation in Drosophila melanogaster. *PLoS Genet* **8**, e1003061 (2012).

70. M. Nakao, Y. Sato, A. Aizawa, H. Kimura, Mode of SUV420H2 heterochromatin localization through multiple HP1 binding motifs in the heterochromatic targeting module. *Genes Cells* **29**, 361-379 (2024).
71. G. Schotta, A. Ebert, G. Reuter, SU(VAR)3-9 is a conserved key function in heterochromatic gene silencing. *Genetica* **117**, 149-158 (2003).
72. D. Canzio, A. Larson, G. J. Narlikar, Mechanisms of functional promiscuity by HP1 proteins. *Trends Cell Biol* **24**, 377-386 (2014).
73. Y. Li, D. A. Kirschmann, L. L. Wallrath, Does heterochromatin protein 1 always follow code? *Proc Natl Acad Sci U S A* **99 Suppl 4**, 16462-16469 (2002).
74. A. Lupo *et al.*, KRAB-Zinc Finger Proteins: A Repressor Family Displaying Multiple Biological Functions. *Curr Genomics* **14**, 268-278 (2013).
75. N. Murzina, A. Verreault, E. Laue, B. Stillman, Heterochromatin dynamics in mouse cells: interaction between chromatin assembly factor 1 and HP1 proteins. *Mol Cell* **4**, 529-540 (1999).
76. D. C. Schultz, K. Ayyanathan, D. Negorev, G. G. Maul, F. J. Rauscher, 3rd, SETDB1: a novel KAP-1-associated histone H3, lysine 9-specific methyltransferase that contributes to HP1-mediated silencing of euchromatic genes by KRAB zinc-finger proteins. *Genes Dev* **16**, 919-932 (2002).
77. S. F. Banani, H. O. Lee, A. A. Hyman, M. K. Rosen, Biomolecular condensates: organizers of cellular biochemistry. *Nat Rev Mol Cell Biol* **18**, 285-298 (2017).
78. Y. H. Ling *et al.*, Disordered C-terminal domain drives spatiotemporal confinement of RNAPII to enhance search for chromatin targets. *Nature cell biology* **26**, 581-592 (2024).
79. A. Patil *et al.*, A disordered region controls cBAF activity via condensation and partner recruitment. *Cell* **186**, 4936-4955 e4926 (2023).
80. A. R. Strom *et al.*, Phase separation drives heterochromatin domain formation. *Nature* **547**, 241-245 (2017).
81. C. M. Koch, M. Honemann-Capito, D. Egger-Adam, A. Wodarz, Windei, the Drosophila homolog of mAM/MCAF1, is an essential cofactor of the H3K9 methyl transferase dSETDB1/Eggless in germ line development. *PLoS Genet* **5**, e1000644 (2009).
82. K. Osumi, K. Sato, K. Murano, H. Siomi, M. C. Siomi, Essential roles of Windei and nuclear monoubiquitination of Eggless/SETDB1 in transposon silencing. *EMBO Rep* **20**, e48296 (2019).
83. R. T. Timms, I. A. Tchasovnikarova, R. Antrobus, G. Dougan, P. J. Lehner, ATF7IP-Mediated Stabilization of the Histone Methyltransferase SETDB1 Is Essential for Heterochromatin Formation by the HUSH Complex. *Cell Rep* **17**, 653-659 (2016).
84. R. S. Kamath, M. Martinez-Campos, P. Zipperlen, A. G. Fraser, J. Ahringer, Effectiveness of specific RNA-mediated interference through ingested double-stranded RNA in Caenorhabditis elegans. *Genome Biol* **2**, RESEARCH0002 (2001).
85. L. Timmons, D. L. Court, A. Fire, Ingestion of bacterially expressed dsRNAs can produce specific and potent genetic interference in Caenorhabditis elegans. *Gene* **263**, 103-112 (2001).
86. K. S. Ghanta, C. C. Mello, Melting dsDNA Donor Molecules Greatly Improves Precision Genome Editing in Caenorhabditis elegans. *Genetics* **216**, 643-650 (2020).
87. C. Dietz, M. R. Berthold, KNIME for Open-Source Bioimage Analysis: A Tutorial. *Adv Anat Embryol Cell Biol* **219**, 179-197 (2016).
88. G. Raiymbek *et al.*, An H3K9 methylation-dependent protein interaction regulates the non-enzymatic functions of a putative histone demethylase. *Elife* **9** (2020).
89. D. Hoogewijs, K. Houthoofd, F. Matthijssens, J. Vandesompele, J. R. Vanfleteren, Selection and validation of a set of reliable reference genes for quantitative sod gene expression analysis in C. elegans. *BMC Mol Biol* **9**, 9 (2008).
90. T. Nolan, R. E. Hands, S. A. Bustin, Quantification of mRNA using real-time RT-PCR. *Nat Protoc* **1**, 1559-1582 (2006).
91. L. Kolberg *et al.*, g:Profiler-interoperable web service for functional enrichment analysis and gene identifier mapping (2023 update). *Nucleic Acids Res* **51**, W207-W212 (2023).

92. J. E. Beaver, M. L. Waters, Molecular Recognition of Lys and Arg Methylation. *ACS Chem Biol* **11**, 643-653 (2016).

Figure 01: MET-2 and HPL-2 colocalize independently into heterochromatic foci

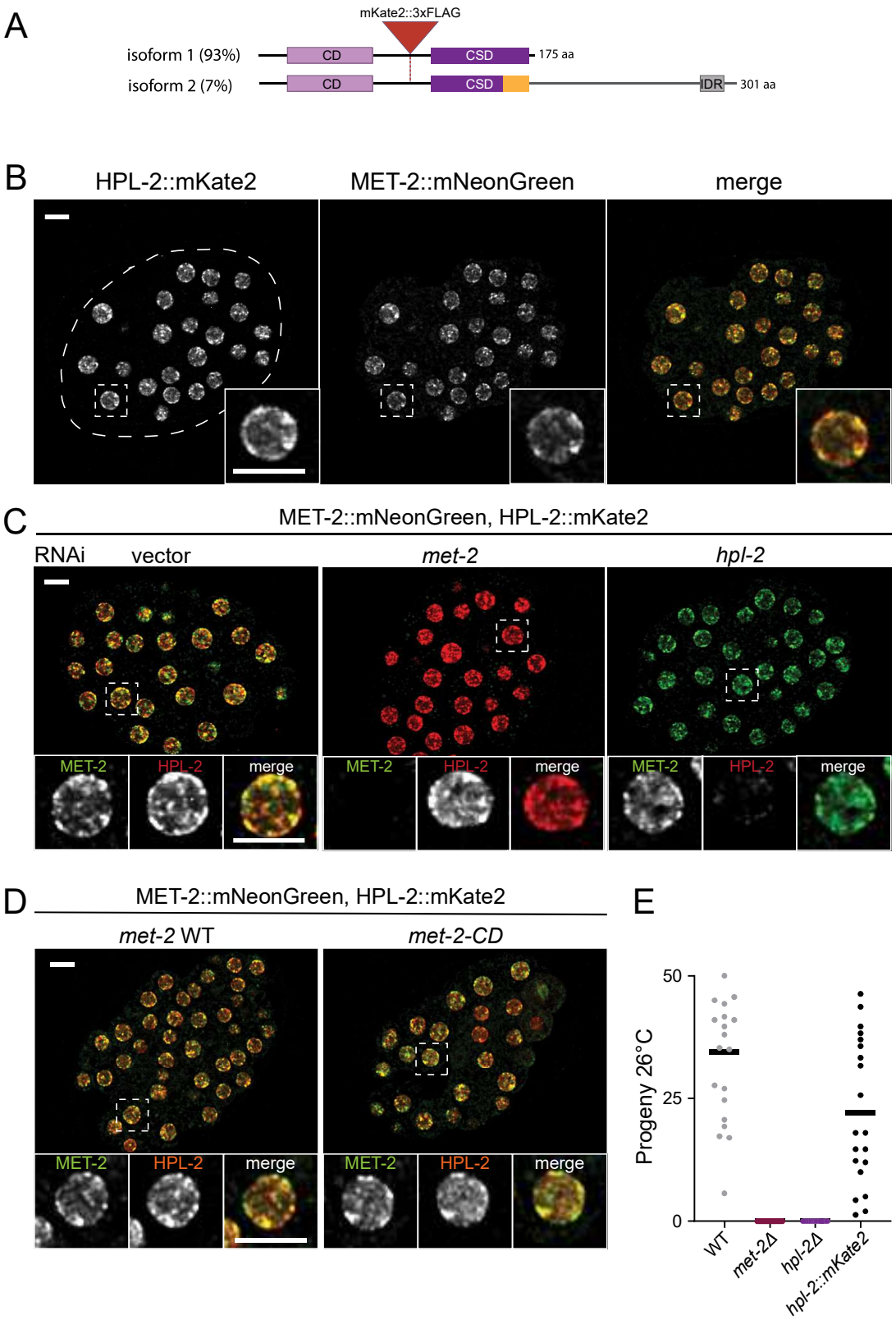

Figure 01: supplement

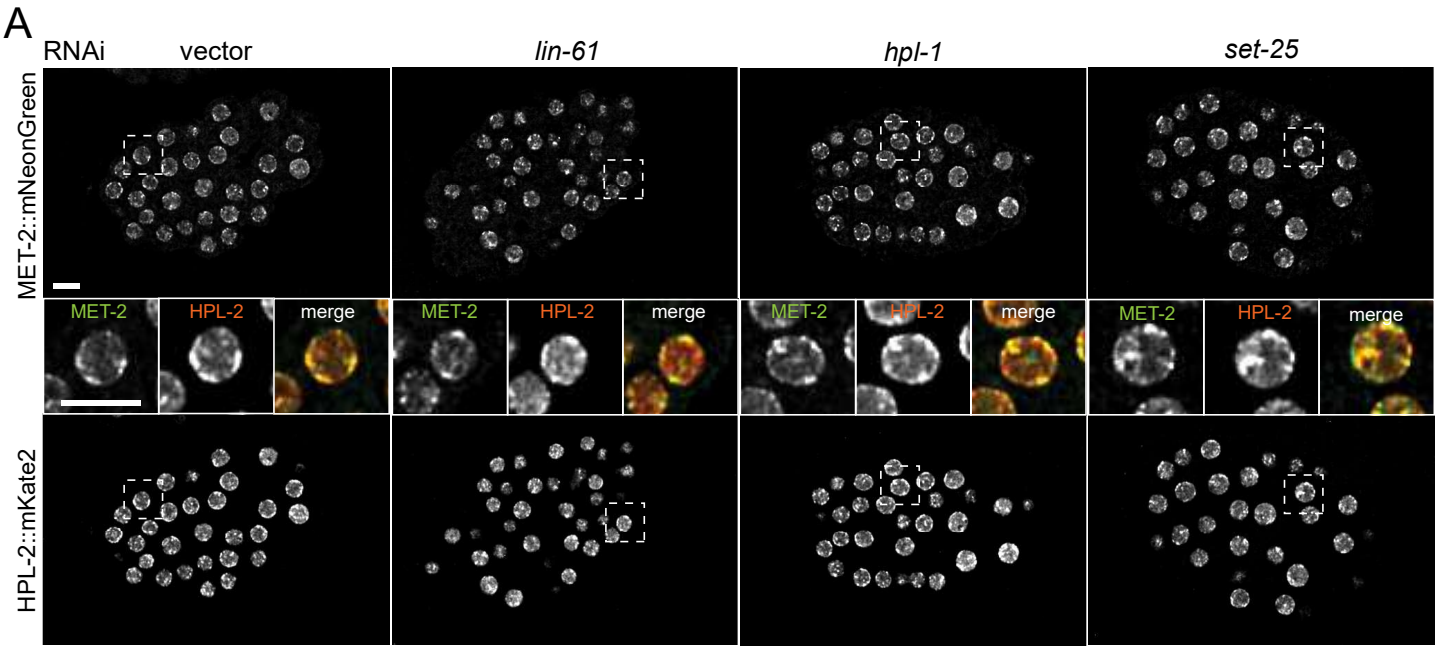

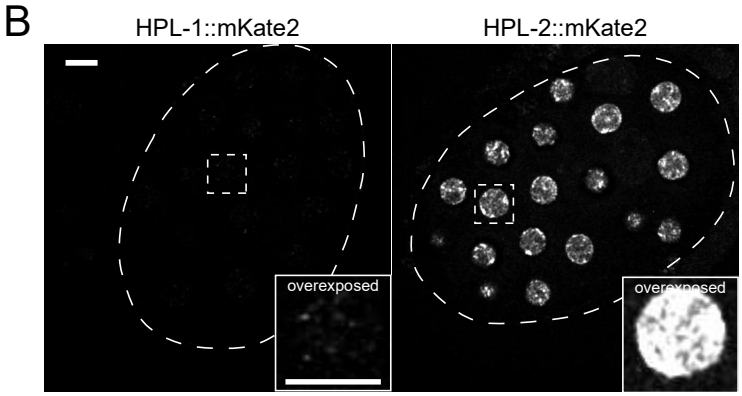

Figure 02: H3K9me and HPL-2 act independently to repress transcription

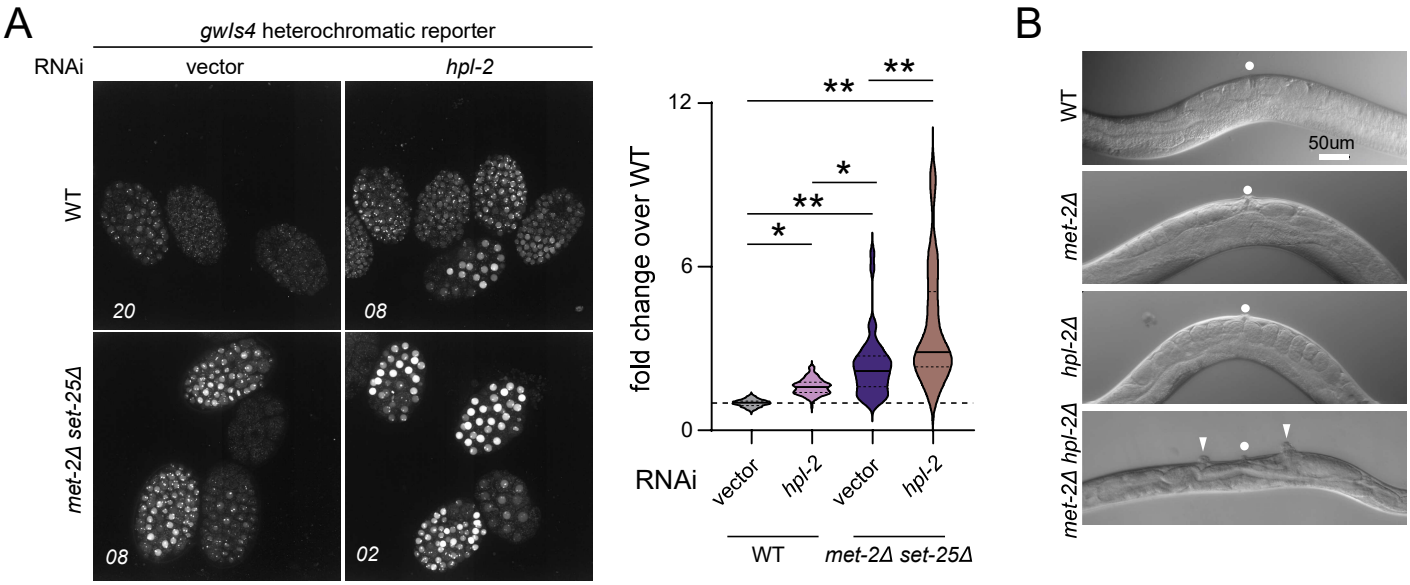

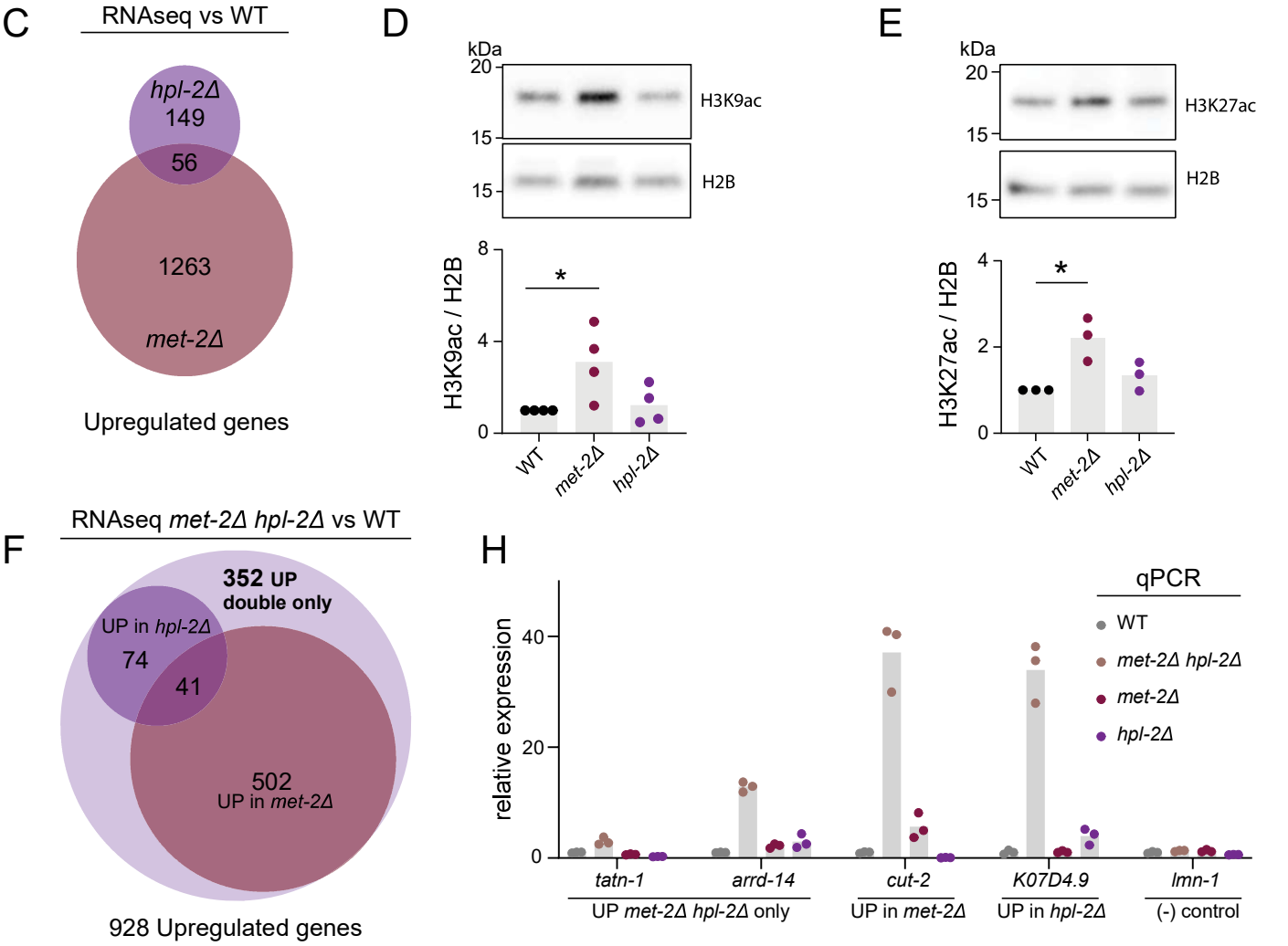

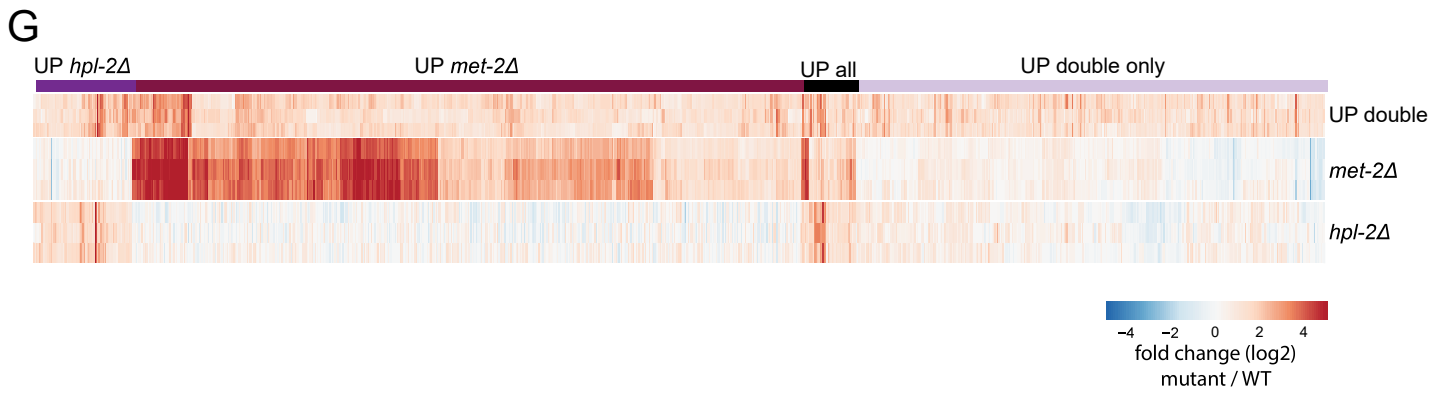

Figure 02: Supplement

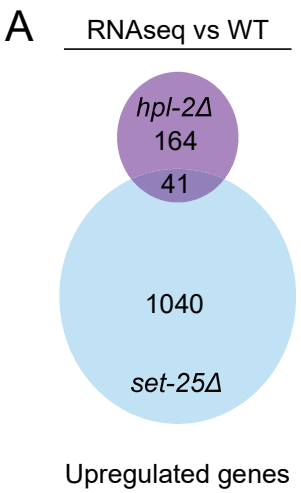

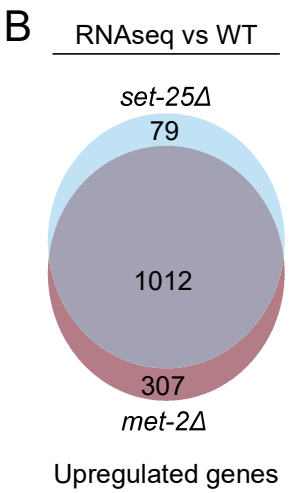

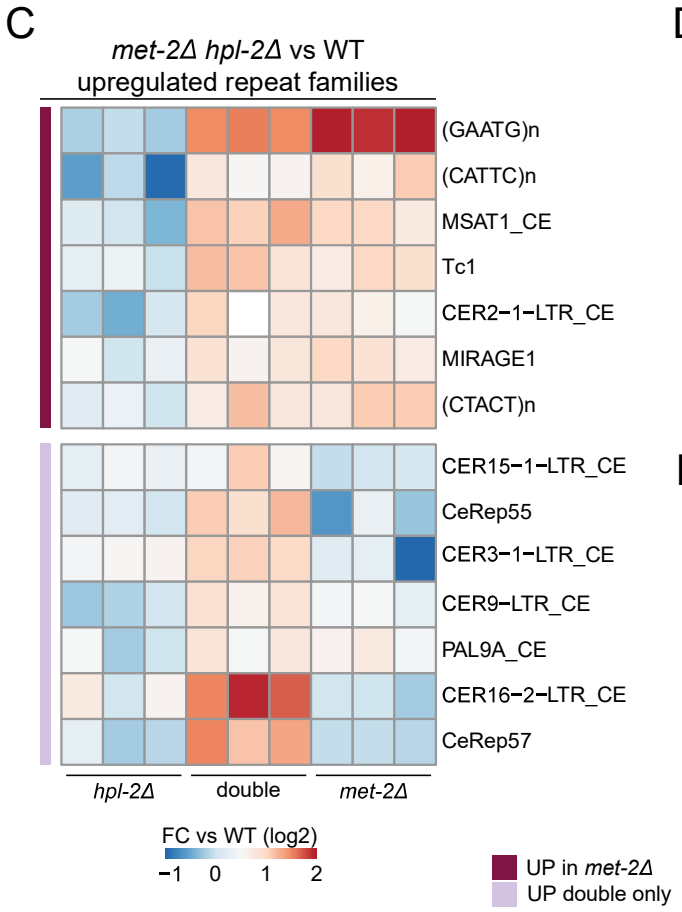

D

GO terms *met-2Δ hpl-2Δ* upregulated genes

term_id	term_name	term_size	intersection_size	p_value
GO:0042744	hydrogen peroxide catabolic process	3	2	5.1e−02
GO:0000786	nucleosome	87	7	6.6e−04
GO:0032993	protein−DNA complex	92	7	9.6e−04
GO:0000785	chromatin	120	7	5.5e−03
GO:0005694	chromosome	181	7	7.0e−02
GO:0030527	structural constituent of chromatin	85	7	3.6e−03
GO:0005198	structural molecule activity	445	14	1.9e−02
GO:0004096	catalase activity	3	2	5.7e−02
GO:0031177	phosphopantetheine binding	3	2	5.7e−02

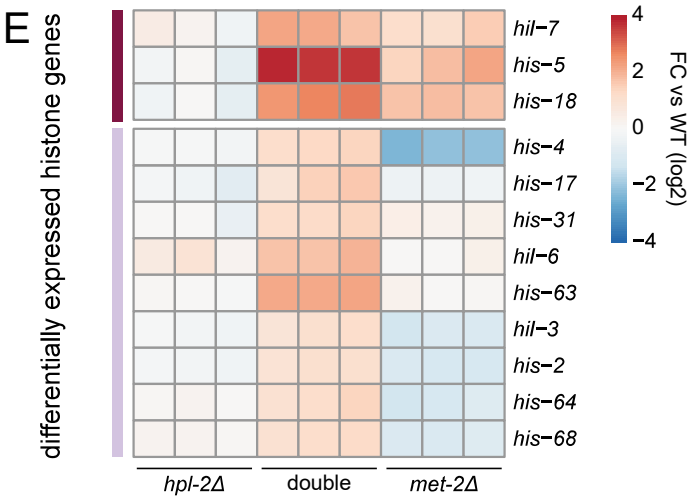

Figure 03: HPL-2 forms nuclear foci independent of H3K9 methylation

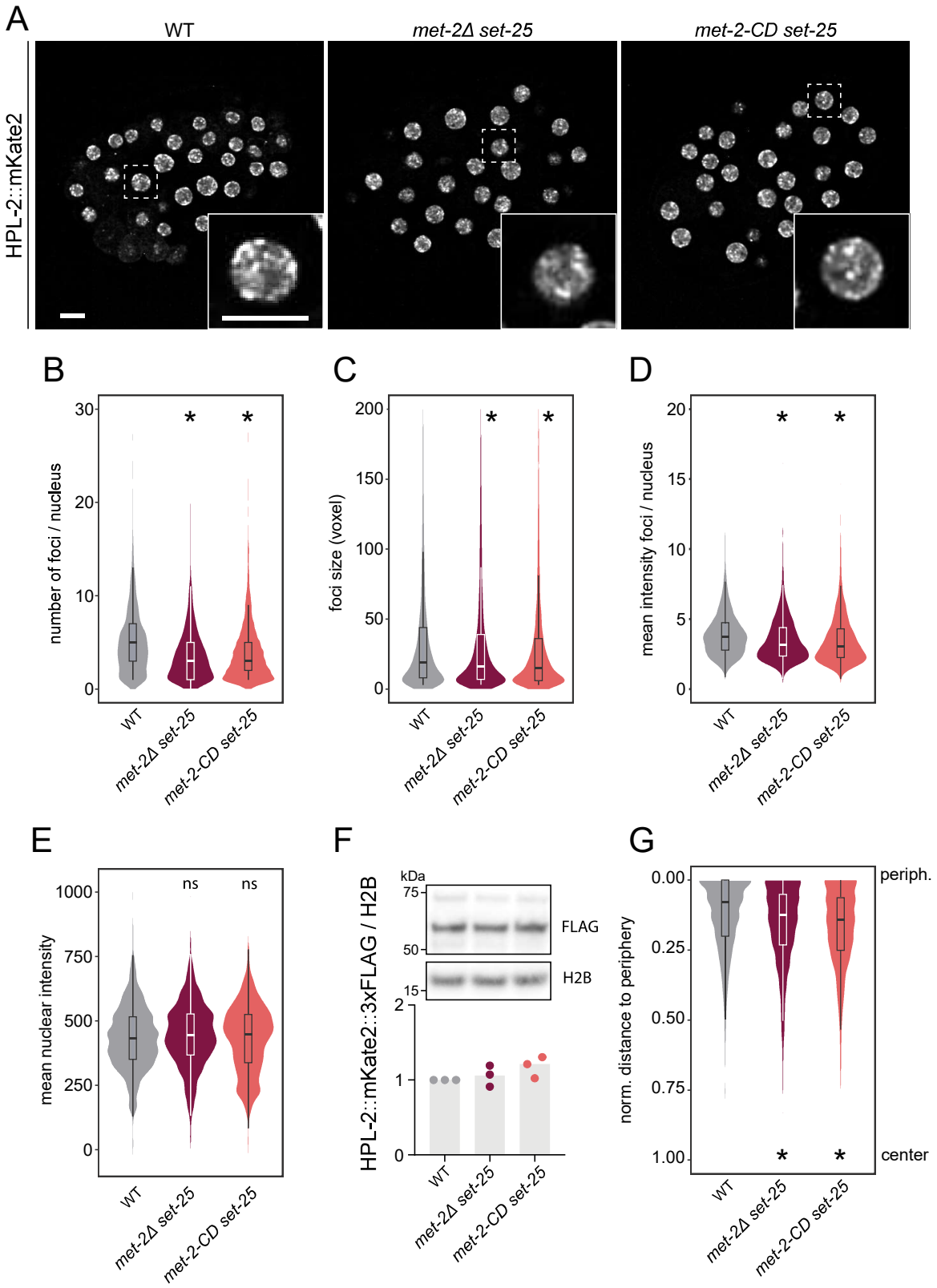

Figure 3:Supplement

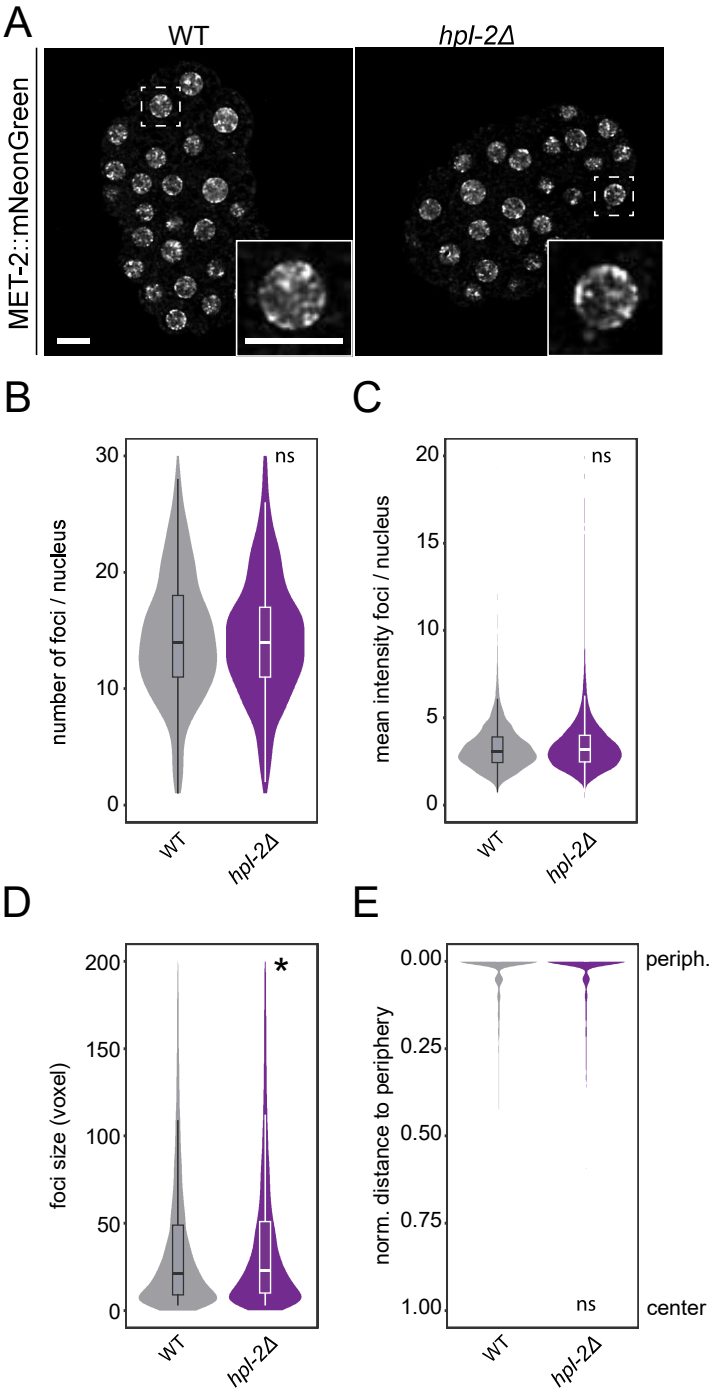

Figure 04: HPL-2 defective in binding H3K9me2/3 represses transcription and suffices for cell identity

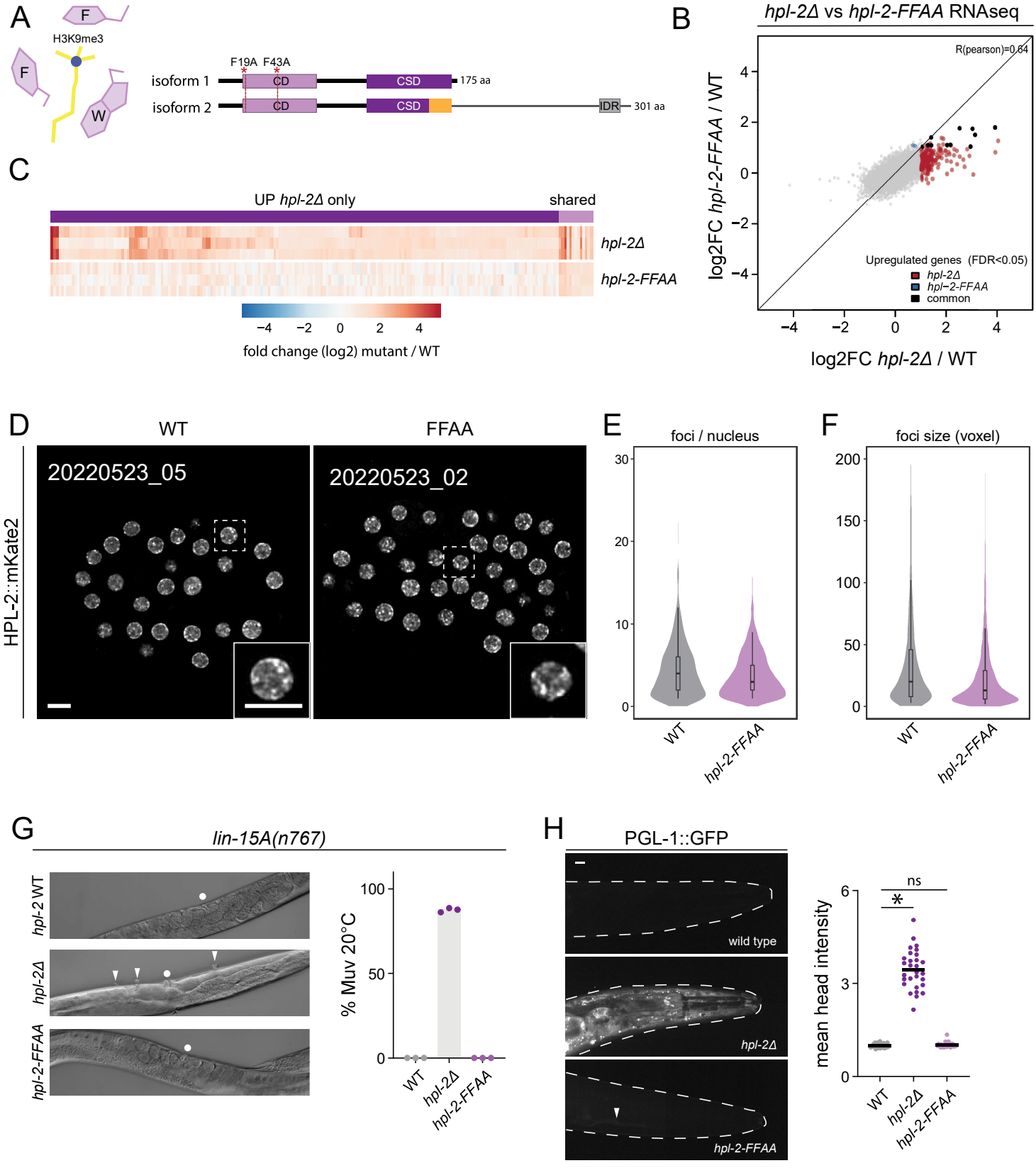

Figure 4: Supplement

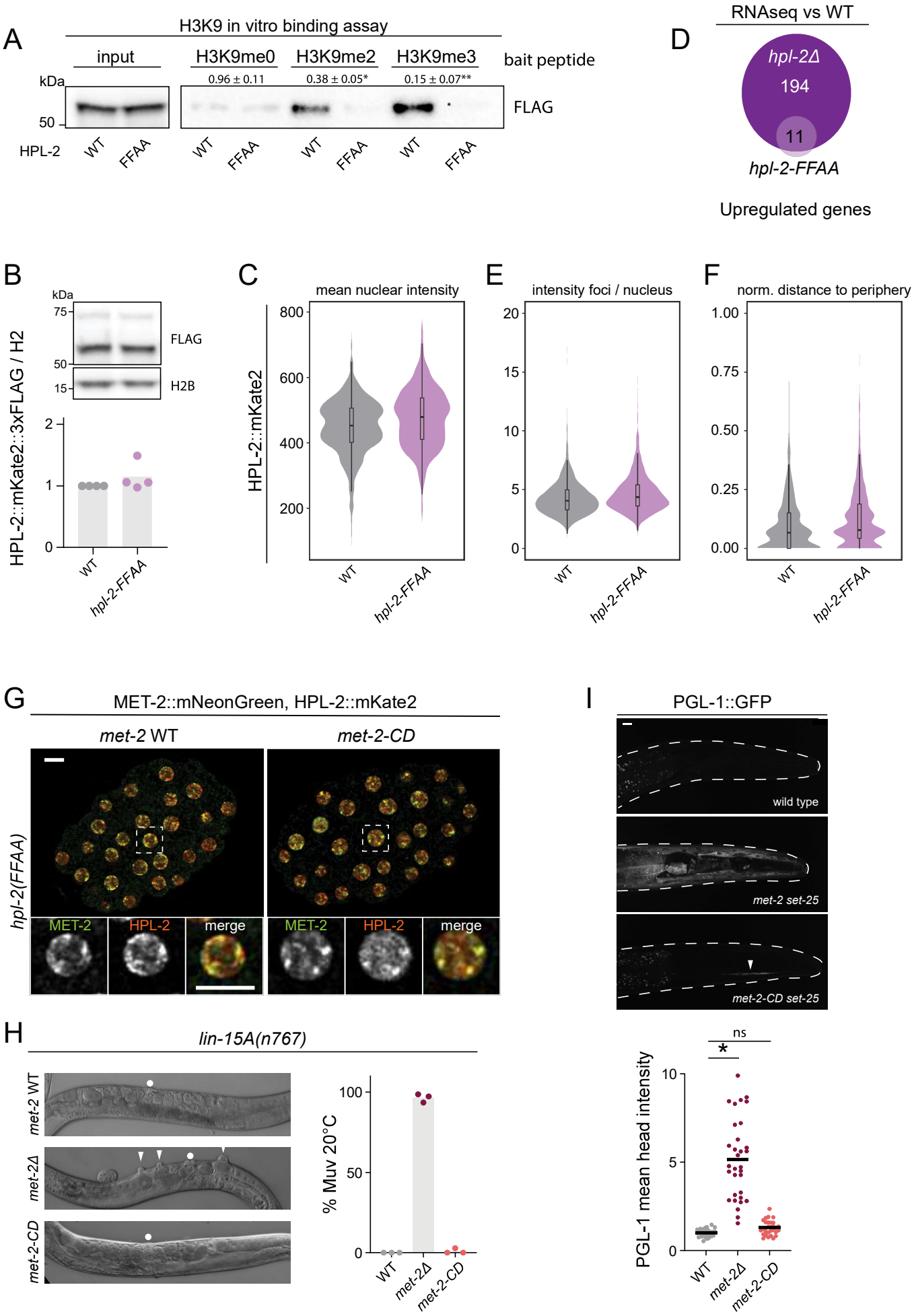

Figure 05: MET-2 and HPL-2 require physical interactions with multvalent cofactors to promote cell fate acquisition

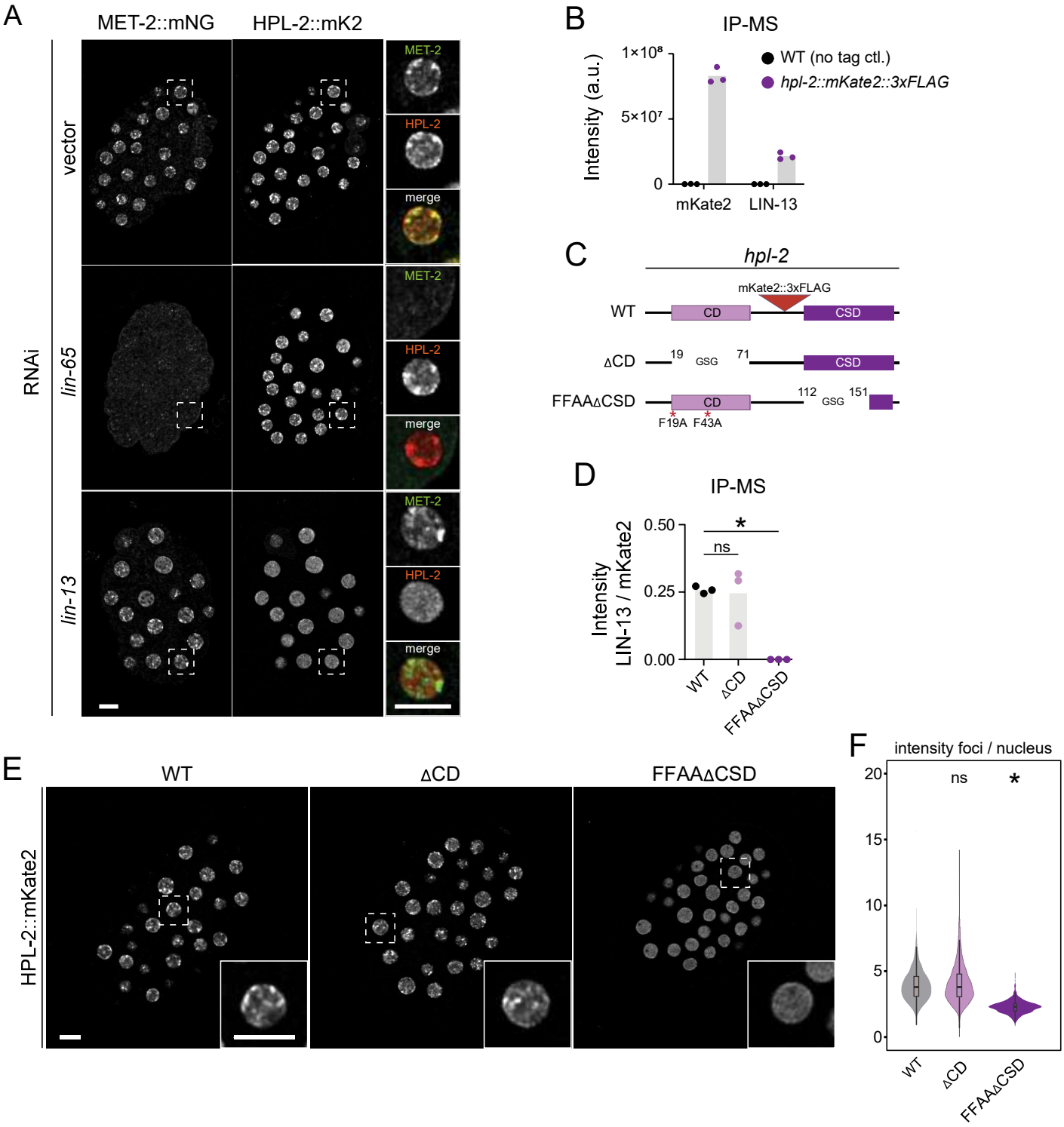

Figure 5: Supplement

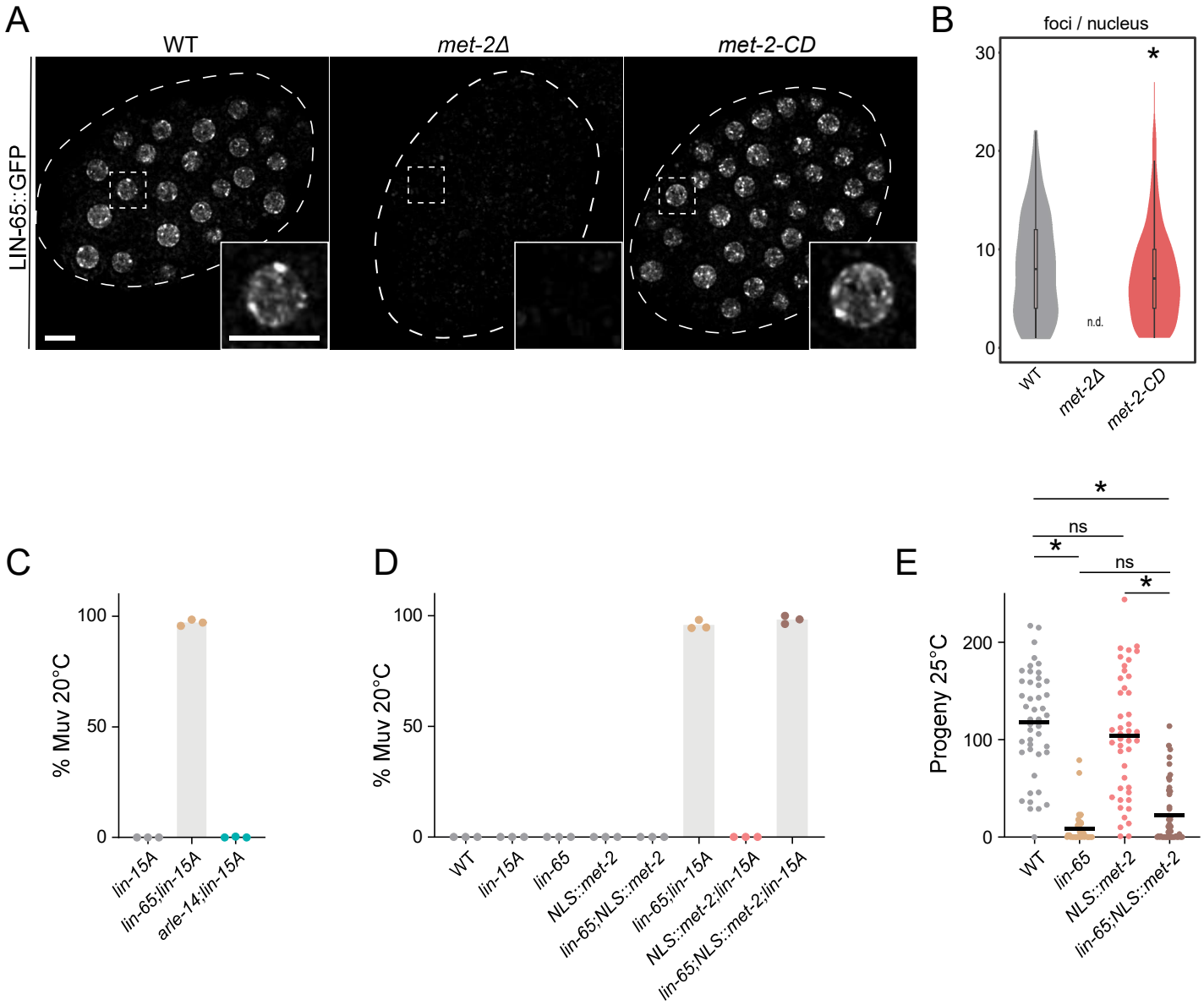
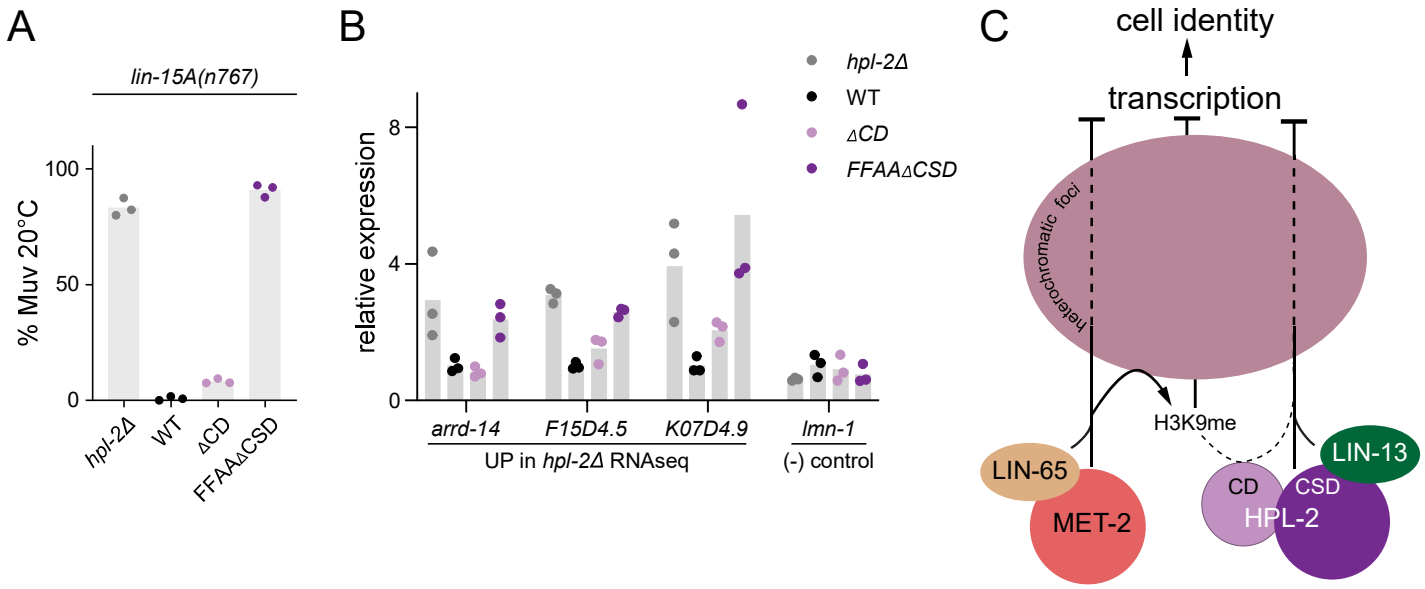
Figure 06: HPL-2 chromoshadow domain is essential for cell fate